BONDING AND DIFFUSIONAL DYNAMICS OF d- AND f-SHELL METALS AND THEIR COMPOUNDS

KAN HACHIYA

1999

A DISSERTATION
PRESENTED TO THE GRADUATE SCHOOL
OF ENERGY SCIENCE
OF KYOTO UNIVERSITY
IN FULFILLMENT OF THE REQUIREMENTS FOR
THE DEGREE OF DOCTOR OF ENERGY SCIENCE

The past is hidden, beyond the reach of intellect, in some material object (in the sensation which that material object will give us) which we do not suspect. And as for that object, it depends on chance whether we come upon it or not before we ourselves must die.

— Marcel Proust. *Swann's Way.*
Translated by C. K. Scott Moncrieff.
Cited in Paul Auster, *The Invention of Solitude.*

Acknowledgements

I have studied here in the Energy Chemistry Laboratory for five years. For the first two years, I studied as a student of the master's course of the Graduate School of Engineering, and for the last three years, as a student of doctor's program of the Graduate School of Energy Science. First and foremost, I thank my thesis advisor Professor Yasuhiko Ito for the kind and continuous encouragement to the present study for all through these five years.

I would like to thank Professor Takeshi Yao and Professor Katsukuni Yoshida for their suggestions, which are of much help to accomplish the present dissertation.

Also, I thank Associate Professor Rika Hagiwara, Dr. Erik O. Ahlgren, Mr. Masayuki Tada, Dr. Koji Amezawa, Dr. Yasushi Katayama, Mr. Takuya Goto, Dr. Toshiyuki Nohira and Professor Kazuhiro Wada for sometimes long and sometimes short discussions. They made me aware of the different point of view on the problems I have been tackled.

And I thank especially Dr. Junya Kondoh for pieces of valuable advice. He infected me with some of his high spirit in materials science. He kindly read preprints of the publications which consist some chapters of the present dissertation, though I could not make use all of the advice.

Dr. Lennart O. Jerdal kindly read the manuscript of one of the publications which has become one chapter and corrected my English.

Sometimes, I spent long time for talking with those who were and who are in Energy Chemistry Laboratory. I owe many ideas and knowledges to them. They helped me in many ways and the words they passed encouraged me.

Professor Nobuhiro Go at the Graduate School of Science of Kyoto University was the first mentor in computational physics when I was a undergraduate student of the Faculty of Science and I am grateful for spending exciting one year in his laboratory.

I found some valuable comments in the short talk with Professor Fumio Hirata at the Institute for Molecular Science, formerly at the Graduate School of Science of Kyoto University, and Professor Bjørn Hafskjold at the Norwegian University of Science and Technology, in the early stage of this study.

A part of the computations in the present study are done at the Kyoto University Data Processing Center and at the Supercomputer Laboratory, Institute for Chemical Research, Kyoto University.

There must be more words for acknowledgements to write. But, they fail me. There are more people I want to express my appreciation. I believe many of them would know how I am filled with gratitude. I wish all of them happiness and success and may them last forever.

KAN HACHIYA

January, 1999

Contents

1 General introduction **3**
- 1.1 Molecular dynamics simulation 5
- 1.2 Hybridized nearly-free-electron–tight-binding -bond model 6
- 1.3 Aim of this study 7

2 Atomistic simulation of the bonding and the self-diffusion in C15 Ni-Y Laves phase structure intermetallic compound **13**
- 2.1 Introduction 13
- 2.2 Computational method 14
  - 2.2.1 Interatomic potential 14
  - 2.2.2 Molecular dynamics calculation 17
- 2.3 Results and discussions 19
  - 2.3.1 Perfect crystal calculation 19
  - 2.3.2 Vacancy structure calculation 20
  - 2.3.3 Grain-boundary structure calculation 23
- 2.4 Conclusions 28

3 Hybridized NFE-TBB model of the bonding in the light-actinide metals **33**
- 3.1 Introduction 33
- 3.2 Computational method 35
- 3.3 Results 37
  - 3.3.1 Potentials for fcc Th 37
  - 3.3.2 Potentials for fcc Pu 39
- 3.4 Conclusions 41

4 Hybridized NFE-TBB model of the bonding in the aluminium metals **45**
- 4.1 Introduction 45

4.2 Potential model and computational method 46
4.3 Results 48
4.4 Conclusions 52

5 Hybridized NFE-TBB model of the bonding in the rare-earth metals 57
5.1 Introduction 57
5.2 Computational method 58
5.3 Results 61
5.4 Conclusions 67

6 Hybridized NFE-TBB model of the bonding in C15 Laves phase structure Al–rare-earth intermetallic compounds 71
6.1 Introduction 71
6.2 Computational method 72
6.3 Results 75
6.3.1 Interatomic Potentials for Al_2Nd 75
6.3.2 Interatomic Potentials for Al_2Pr 78
6.4 Conclusions 80

7 General conclusion 83

A Distribution of the valence electrons in binary transition-metal alloys 91

B Tight-binding approximations of the vacancy formation energy in binary transition-metal alloys 97

List of Figures

1.1 Schematics of the fcc, hcp, dhcp and C15 Laves phase structures. . 8

2.1 Dependence of the bond order for the bondings in the bulk structure to the number of moment. 16
2.2 Effective interatomic potential for Ni-Ni, Ni-Y and Y-Y interactions and interatomic potential for sp and d interactions for Ni-Ni . 18
2.3 Radial distribution functions for Ni-Ni at 773K. 20
2.4 Mean square displacements at 773K. 21
2.5 Spectral densities of velocity for Ni and Y at 773K. 22
2.6 Spectral densities of velocity for Ni and Y at 773K. 23
2.7 Examples of the atomic motions near Ni vacancy projected onto a two dimensional plane. 24
2.8 The model for molecular dynamics simulation for a grain-boundary structure in Ni_2Y phase. The schematic of the computational cell and the projected atomic arrangements. 25
2.9 Mean square displacements at 773K. 26
2.10 Radial distribution function for the grain-boundary structure at 773K calculated from $1/10$ sample coordinates in additional $3\,000$ time steps simulation 27
2.11 Spectral densities of velocity for Ni and Y at 773K in the grain-boundary structure calculated from $1/10$ sample velocities in additional $3\,000$ time steps simulation. 28
2.12 Variation of the horizontal and the vertical self-diffusion coefficients versus z axis neutral to grain-boundary. 29

3.1 Schematic of the bonding and the bond angles and the angular dependence of the embedding function $g(\theta)$. 37
3.2 Interatomic potential for fcc Th at 0K. Potential energy curve toward first-nearest-neighbour bond direction. 38

3.3 Binding energy per atom as function of γ for tetragonally and trigonally deformed fcc Th. 39
3.4 Interatomic potential for fcc Pu at 0K. Potential energy curve toward first-nearest-neighbour bond direction. 40

4.1 Interatomic potential for Al at 0K. Potential energy curve toward first-nearest-neighbour bond direction. 50
4.2 Change of the binding energy per atom as function of γ for tetragonally and trigonally deformed fcc Al. 51

5.1 Interatomic potential for β-La calculated with the final set of parameters. 62
5.2 Change of the binding energy per atom as function of γ for tetragonally and trigonally deformed β-La. 63
5.3 Plots of the experimental versus calculated elastic constants for C_{66}, C_{44}, C_{S} and C_{33}. 66

6.1 Interatomic potential for Al_2Nd calculated with the final set of parameters. 76
6.2 Change of the binding energy per atom as function of γ for tetragonally and trigonally deformed Al_2Nd. 77
6.3 Change of the binding energy per atom as function of γ for tetragonally and trigonally deformed Al_2Pr. 79

A.1 Schematic of the rectangular d-band model of the binary transition-metal alloy formation. 93

B.1 Bond order change for the bondings near Ni and Y vacancy within second moment approximation. 99

List of Tables

2.1 NFE potential parameters for Ni_2Y perfect crystal. 15
2.2 Bond order for covalent d-d interactions in Ni_2Y phase within angular dependent second moment approximation. 16

3.1 Calculated coefficients for the angularly dependent embedding function. 36
3.2 Calculated and experimentally determined elastic constants of α-Th at 0K. 39
3.3 Calculated and experimentally determined elastic constants of fcc Pu at room temperature. 41

4.1 The results of the fitting of the adjustable parameters. 49
4.2 Calculated and experimentally determined elastic constants C_{ij}, the result of the fitting and the experimental data for the interatomic separations d and the bulk moduli B for the fcc Al at 0K. . 49
4.3 Energy differences for bcc and hcp structures compared with fcc structure. 52

5.1 Number of valence electron used in the present calculations and the final values of the interatomic potential parameters for the rare-earth metals derived by fitting to the experimental data of the elastic constants. 62
5.2 Calculated and experimentally determined elastic constants C_{ij}, the result of the fitting and the experimental data for the interatomic separations d and the bulk moduli B for the cubic crystals. 64
5.3 Calculated and experimentally determined elastic constants C_{ij}, the result of the fitting and the experimental data for the interatomic separations d and the bulk moduli B for the hexagonal crystals. 65

6.1 Adjusted interatomic potential parameters for Al_2Nd phase at 300K. 75
6.2 Calculated elastic constants and results of the fitting of the bulk modulus and the interatomic separations for Al_2Nd at 300K. . . . 76
6.3 Adjusted interatomic potential parameters for Al_2Pr phase at 300K. 78
6.4 Calculated elastic constants and results of the fitting of the bulk modulus and the interatomic separations for Al_2Pr at 300K. 78

B.1 Vacancy formation energy for Ni and Y in Ni_2Y phase for the M-th moment approximation. 98

Chapter 1

General introduction

Let us begin with a little long citation;

> If, in some cataclysm, all of scientific knowledges were to be destroyed, and only one sentence passed on to the next generations of creatures, what statement would contain the most information in the fewest words? I believe it is the *atomic hypothesis* (or the atomic *fact*, or whatever you wish to call it) that *all things are made of atoms — little particles that move around in perpetual motion, attracting each other when they are a little distance apart, but repelling upon being squeezed into one another.* In that sentence, you will see, there is an *enormous* amount of information about the world, if just a little imagination and thinking are applied.

This famous statement of Richard Feynman in the opening chapter of his textbook [1] perfectly describes the main theme of the science at the first half of this century, and remains to be true in the materials science still now.

Diffusion problem is closely connected to the atomistic viewpoint of the materials by nature. Brownian motion, which is the elementary process of the diffusion, was taken into a framework of the theory by Einstein [2] at the beginning of this century, where he interpreted the motion as a molecular motion. This theory established the basic foundation of the atomic theory of matter in the meaning that it connects the heat with molecular motion [3] and this is an early example of the fluctuation-dissipation theorem.[1]

[1] Einstein's theory is also the beginning of the theory of stochastic process. Richard Feynman made a great contribution to the quantum mechanics [4] with the theory of stochastic process.

In the context of the fluctuation-dissipation theorem, the formula known as the Einstein relation gives the relation between the diffusion constant D of the Brownian particle and the mobility μ by

$$D = \mu k_{\mathrm{B}} T \tag{1.1}$$

and states that the diffusion constant is proportional to a kind of the friction constants (the ratio of the drift velocity to the external force) which determines the energy dissipation. The diffusion constant D is written as

$$D = \frac{1}{3} \int_0^\infty dt \, \langle v(t) \cdot v(0) \rangle, \tag{1.2}$$

which means that the zero frequency spectrum of the fluctuations of the velocity in thermal equilibrium gives the diffusion constant.

The present dissertation accounts for the diffusion in materials from the atomistic point of view, which is driven by the random force that seems to act by chance in our ordinary sense, and the origin of the random force itself and the frictional force, chemical bondings between atoms[2]. This approach arises not only from the theoretical necessity as we have seen below, but from the practical viewpoint. The acceleration of the atomic transport in the solid state materials such as metals or alloys is one of the central problems in energy conversion processes. Diffusion, very often, determines the speed of the atomic transport, and therefore determines the efficiency. The key to our understanding of the mechanism of the transport process must be sought in the combination of the constituent elements or in the complex interatomic interactions mediated by chemical bondings.

The present dissertation tackles these problems with the atomistic simulations, molecular dynamics simulation of the self-diffusional dynamics in the transition-metal intermetallic compounds, and the optimization of the semi-empirical potentials descriptions of the bondings in d- and f-shell metals and their compounds, by means of the hybridized nearly-free-electron–tight-binding-bond model potential. Overview of these methods are given in the following sections and aim of this study is summarized in the last section in this chapter. Applications to each problems are discussed from the next chapter.

[2]This is not the only origin of the force acts on Brownian particle. As we see later, the total force from the potential can be divided into random force and frictional force together with the random force from the heat bath.

1.1 Molecular dynamics simulation

In the last few decades, wider and wider problems in the materials science have come into the applicability of the atomistic simulations because of the rapid growth of the computational power. At the same time, our understanding of the bonding — the central problem in the atomistic simulations — also becomes deepened and we can now express and calculate the same properties more simply and more exactly compared with the decades ago. One of the most outstanding progress in atomistic simulation is Car-Parrinello method [5], which calculates force acting on an atom through the electronic structure calculation based on the density functional method [6] and describes both atomic and electron density dynamics. This method can be said as a kind of variation of the method to calculate the dynamical structure of a system based on Newtonian dynamics, which is known as Molecular Dynamics (MD) simulation.

The MD simulation, ranging from the purely classical dynamics to the first-principles method such as Car-Parrinello method, has a wide variety of applications including structure optimization, mechanical properties simulation, lattice dynamics, and so on. Transport properties simulation is one of the most natural selection of the application of this method, as it is directly connected to the dynamical structure of a system to be calculated with MD simulation.

In the actual description of the time evolution in MD, a set of equations called Nosé-Hoover equations of motion [7, 8] are commonly used to introduce temperature for the simulated system.

$$m_i \dot{\boldsymbol{v}}_i = \boldsymbol{F}_i - \zeta m_i \boldsymbol{v}_i \tag{1.3}$$

$$\dot{\zeta} = 2(K - K_0)/Q, \tag{1.4}$$

where K is the kinetic energy of the system and K_0 is the kinetic energy corresponding to the temperature of the system. This set of equations contains a pseudofrictional force $-\zeta m v$ in addition to the real force F acting on an atom. This force can be both positive and negative and the simulated system can exchange energy between heat bath through ζ to maintain constant temperature. We can obtain canonical average of a physical quantity by calculating time average of a physical quantity which is expressed by the coordinates generated by above equations if the ergodic hypothesis is fulfilled.

For a realistic simulation, it is important to choose efficient and physically appropriate interatomic potentials functions and also important to optimize Q in equation 1.4. The adjustable parameter, Q can be written as $Q = 3(N-1)k_B T \tau^2$

where N is the number of atoms in system [9]. In this formula, τ is the adjustable relaxation time for the system. If we set too large value to τ, the simulated system is coupled to heat bath too weakly and reaches to equilibrium too slowly. If we set too small value, the system is too closely coupled to heat bath and the natural dynamics of the atoms is replaced by the highly constrained dynamics.

The determination of Q has more or less empirical character, but some practical procedure is provided by Holian et al [10].

1.2 Hybridized nearly-free-electron–tight-binding - bond model

Atomistic simulations, especially MD simulations, depend largely on the choice of the interatomic potentials, because most of the computation time is consumed with the calculation of the force acting on atoms, and because the constituent atoms in the simulating materials are characterized by the bondings they form with the surrounding atoms.

At the early stage of the development, empirical interatomic potentials function such as 12-6 Lennard-Jones potentials or Tosi-Fumi potentials are used for the molecular simulations for the limitations of the computational resources [11]. As the performance of the computers have been improved, the range of the field to which molecular simulations can be applied has been increased with the improvement of the description of the interatomic interactions through semi-empirical potentials models [12]. The interactions in these models depend not only on the interatomic separations but on the environment of the particular bond or the nature of the bond itself. These improvements are essential for the metals and their compounds as bondings in such materials have many-atom character and for the covalent bond materials and semi-conductors as their bondings are strongly angular-dependent because of the shape of the orbitals. Even though the first-principles calculations have become applicable to the wider and wider materials in these days, there still remains a great importance for the semi-empirical model of the bondings especially for the large-scale and long time-scale simulations such as those for dynamical and mechanical properties of the materials.

The present dissertation treats the bondings in the d- and f-shell metals and their compounds. The valence electrons in these metals and compounds are divided into free-electron-like sp- or spd-electrons and tight-binding d- or f-electrons. Based on this picture, Wills and Harrison developed an interatomic interactions

model and successfully predicted the trends in the cohesive properties of d- and f-shell metals [13, 14, 15]. Hausleitner and Hafner developed a more realistic and quantitative interatomic interactions model based on the same picture as the Wills and Harrison's model for transition-metals and their alloys [13] and transformed it into the simple but exact semi-empirical potentials function for the molecular dynamics simulation [16]. This model, which is known as the hybridized Nearly-Free-Electron–Tight-Binding-Bond (NFE-TBB) model, basically results in pair-wise potential including properties of the environment of a bond through Bethe lattice approach. This is also the case for the widely-used embedded atom model potential [17, 18], which includes properties of the environment through coordination number. As shown in the following chapters, the hybridized NFE-TBB model potential can be a both efficient and physically appropriate potential model that accounts for the many-atom non-pairwise character of the bonding, combined with the bond order formulation by the Bond Order Potential (BOP) [19].

The hybridized NFE-TBB model potential divides a total potential energy function into three parts;

$$\Phi_{\mathrm{total}} = \Phi_{\mathrm{NFE}} + \Phi_{\mathrm{TB,rep}} + \Phi_{\mathrm{TB,bond}}. \tag{1.5}$$

Namely, NFE part, TB repulsive part and TB bonding part. The TB bonding part can be written as

$$\Phi_{\mathrm{TB,bond}} = 2\sum_{\alpha\beta} H_{j\beta,i\alpha}\Theta_{i\alpha,j\beta}, \tag{1.6}$$

and many-atom character enters from the bond order Θ. The success of the potential depends on the choice of the values for the adjustable parameters set in the potential and the choice of the formulation of the bond order.

1.3 Aim of this study

The present dissertation accounts for the bonding and diffusional dynamics of d- and f-shell metals and their compounds. The aim of this study is to reveal the validity and the nature of the hybridized NFE-TBB model of the bondings in these materials which have the principal crystal structures presented in figure 1.1 for the purpose of the application for the molecular dynamics simulations of the dynamical structure study.

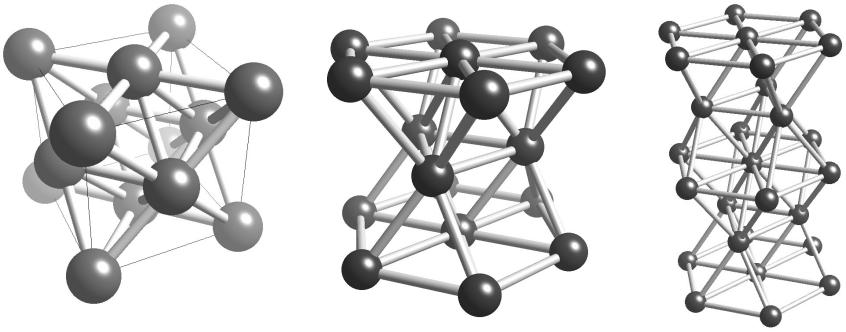

(*a*) (*b*) (*c*)

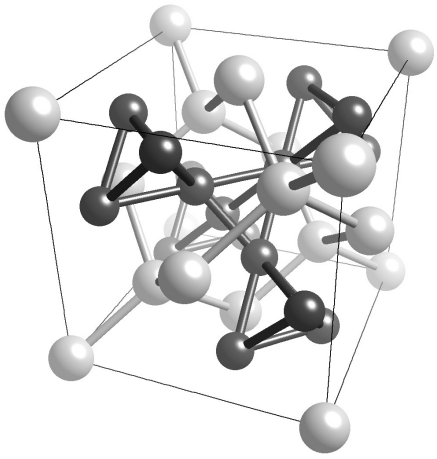

(*d*)

Figure 1.1 Schematics of the (*a*) fcc, (*b*) hcp, (*c*) dhcp and (*d*) C15 Laves phase structures.

A concrete example of the application for the molecular dynamics simulation study on the self-diffusional dynamics in Ni-Y Laves phase intermetallic compound is presented in chapter 2 with the known potential parameters.

Derivation and test of the hybridized NFE-TBB model potential is demonstrated for particular systems from chapter 3 to 6.

The original model for the transition-metals and their alloys is extended to light-actinide metals in chapter 3.

The model originally designed for the transition-metals is successfully applied to aluminium metal in chapter 4 and to rare-earth metals in chapter 5.

A procedure for transferring potential parameters for pure metals obtained in chapter 4 and 5 into aluminium–rare-earth Laves phase intermetallic compounds is presented in chapter 6.

Conclusion of the present study is given in chapter 7.

References

[1] R. P. Feynman, R. B. Leighton and M. L. Sands, *The Feynman Lecture on Physics* Vol. I, (Addison-Wesley, Reading, 1965).

[2] A. Einstein, *Investigations on the Theory of the Brownian Motion*, edited by R. Fürth (Dover, New York, 1956).

[3] R. Kubo, M. Toda and N. Hashitsume, *Statistical Physics II, Nonequilibrium Statistical Mechanics*, 2nd ed. (Springer, Berlin, 1992).

[4] R. P. Feynman and A. R. Hibbs, *Quantum Mechanics and Path Integrals* (McGraw-Hill, New York, 1965).

[5] R. Car and M. Parrinello, *Phys. Rev. Lett.* **55** 2471 (1985).

[6] W. Kohn and L. J. Sham, *Phys. Rev.* **140** A1133 (1965).

[7] S. Nosé, *J. Chem. Phys.* **81** 511 (1984); *Mol. Phys.* **52** 255 (1984).

[8] W. G. Hoover, *Phys. Rev.* A**31** 1695 (1985).

[9] D. J. Evans and B. L. Holian, *J. Chem. Phys.* **83** 4069 (1985).

[10] B. L. Holian, A. F. Voter and R. Ravelo, *Phys. Rev.* E**52** 2338 (1995).

[11] M. P. Allen and D. J. Tildesley, *Computer Simulation of Liquids* (Oxford University Press, Oxford, 1987).

[12] A. E. Carlsson, *Solid State Phys.* **43** 1 (1990).

[13] J. M. Wills and W. A. Harrison, *Phys. Rev.* B**28** 4363 (1983).

[14] W. A. Harrison, *Phys. Rev.* B**28** 550 (1983).

[15] G. K. Straub and W. A. Harrison, *Phys. Rev.* B**31** 7668 (1985).

[16] Ch. Hausleitner and J. Hafner, *Phys. Rev.* B**45** 115 (1992).

[17] M. S. Daw and M. T. Baskes, *Phys. Rev.* B**29** 6443 (1984).

[18] M. W. Finnis and J. E. Sinclair, *Phil. Mag.* A**50** 45 (1984).

[19] M. Aoki, *Phys. Rev. Lett.* **71** 3842 (1993).

Chapter 2

Atomistic simulation of the bonding and the self-diffusion in C15 Ni-Y Laves phase structure intermetallic compound

2.1 Introduction

The acceleration of the atomic transport in the solid state materials is often one of the central problems in energy conversion processes. Diffusion, very often, determines the speed of the atomic transport, and therefore determines the efficiency.

Ni_2Y is the transition-metal intermetallic compound with cubic Laves phase structure and its anomalously high growth rate in electrolysis was found by electrochemical experiments [1]. The Ni-Y intermetallic compound is formed by electrodeposition of Y at the Ni electrode in the molten LiCl-KCl-NaCl-YCl_3 and the Ni_2Y phase selectively grows among competing phases with the growth rate of 10μm h^{-1} at 773K, which is 600K below the melting point.

This high growth rate means that the speed of the atomic transport for the atomic species in this intermetallic phase is of the order of 10^{-12}m^2 s^{-1} as the diffusion coefficient [1]. This is comparable to or only few order smaller than those in the standard liquid phase, which are approximately 10^{-9}m^2 s^{-1} as the diffusion coefficient, or in the common solid phase near melting point, which are 10^{-11}m^2 s^{-1} [2].

How can such anomalously rapid growth of the intermetallic phase take place?

There are several models to describe the atomic diffusion in standard solids; diffusion process via vacancy, dislocation, grain boundary and so on [3]. To which model the diffusion process in this phase is ascribed?

This chapter presents a study of the microscopic dynamic structure of Ni_2Y phase through atomistic simulation, a molecular dynamics simulation, in the investigation of the high growth rate of this intermetallic phase.

Concerning the molecular dynamics technique, a semi-empirical method for the interatomic potential calculation has recently been developed [4] and wide range of materials has come into applicability of the atomistic simulation. Chemical bondings in transition-metal alloy compounds is well-described within the hybridized NFE-TBB (Nearly-Free-Electron–Tight-Binding-Bond) framework [5] and its TBB part can be calculated by the semi-empirical method exact enough to express the many-atom character of interactions in transition-metal intermetallic compounds and computationally fast enough to be used in the intensive molecular dynamics run.

In the present chapter, the calculation of pair potential with the application of the NFE-TBB many-atom interaction model is demonstrated and then used for the calculation of the many-body forces in molecular dynamics calculation.

The computational methods used are outlined in section 2.2. The results of the applications to the self-diffusive motion in vacancy, grain-boundary structures for Ni_2Y are shown in section 2.3. We present our conclusions in section 2.4.

2.2 Computational method

2.2.1 Interatomic potential

For the interatomic potential for Ni_2Y, hybridized NFE-TBB expression developed by Hausleitner and Hafner [5] is used.

$$\Phi_{\mathrm{tot}}(r) = \Phi_{\mathrm{sp}} + \Phi_{\mathrm{d,rep}} + \Phi_{\mathrm{d,bond}}. \tag{2.1}$$

The potential energy is divided into free-electron-like interaction, pairwise repulsive interaction and many-atom attractive bond energy.

The following NFE interaction formulation by Pettifor and Ward [6] is adopted as the first term in equation 2.1;

$$\Phi_{\mathrm{sp}}(r_{ij}) = \frac{2N_{\mathrm{s},i}N_{\mathrm{s},j}}{r_{ij}} \sum_{n=1}^{3} A_n \cos(k_n r + \alpha_n) \exp(\kappa_n r_{ij}). \tag{2.2}$$

$N_{\mathrm{s},i}$ is the number of sp-valence electrons for the i atom. Calculated parameters for the perfect Ni_2Y crystal are compiled in table 2.1. As in reference[6], Ashcroft empty core pseudopotential [7] is used to calculate these parameters.

Table 2.1 NFE potential parameters for Ni_2Y perfect crystal. The values are indicated in atomic unit.

	Ni-Ni			Ni-Y			Y-Y		
n	1	2	3	1	2	3	1	2	3
k_n	0.303	1.144	1.695	0.320	0.901	1.285	0.291	0.731	0.995
κ_n	1.415	1.227	0.494	1.134	0.897	0.371	0.919	0.671	0.283
A_n	8.586	1.533	0.039	5.818	1.566	0.045	2.567	0.948	0.026
α_n	−1.407	−3.785	1.154	−1.297	−3.470	1.346	−1.022	−2.651	2.543

The remaining two terms in equation 2.1 are described within the tight-binding theory [8].

Repulsive interaction is known to be proportional to r^{-10}, the square of hopping integral, but in this study, r^{-8} form is used as in reference [9]. The following is the repulsive interaction used;

$$\Phi_{\mathrm{rep}}(r_{ij}) = \frac{\sqrt{N_{\mathrm{d},i}N_{\mathrm{d},j}}}{7}\frac{h_{ij}^2 d_{ij}^{10}}{r_{ij}^8}. \tag{2.3}$$

h_{ij} is the bond integral and it is calculated in the same way as in reference [10]. d_{ij} is the interatomic spacings. The calculated h_{ij} values for the Ni_2Y are as follows; $h_{\mathrm{NiNi}} = 0.019\,64, h_{\mathrm{NiY}} = 0.029\,38, h_{\mathrm{YY}} = 0.078\,43$ in Ry.

Bond energy expression is;

$$\Phi_{\mathrm{bond}}(r_{ij}) = 2\sum_{\alpha\beta} H_{j\beta,i\alpha}\Theta_{i\alpha,j\beta}. \tag{2.4}$$

$H_{j\beta,i\alpha}$ is the tight-binding Hamiltonian and $\Theta_{i\alpha,j\beta}$ is the bond order. Bond order is calculated from the following simplified expression derived by Pettifor and Aoki [11];

$$\Theta_{i\alpha,j\beta} = 2\sum_{n=2}^{\infty}\widehat{\chi}_n(N_{\mathrm{d}})\zeta_n^r/b^{n-1}. \tag{2.5}$$

$\widehat{\chi}_n(N_{\mathrm{d}})$ is the reduced susceptibility, ζ_n^r is the interference term in the ring approximation and b is the square root of the second moment μ_2, calculated from the tight-binding Hamiltonian [12]. Calculated bond order for each bonding in

perfect Ni_2Y crystal with equation 2.5 within the second moment approximation is compiled in table 2.2 and up to sixth moment approximation results are presented in figure 2.1.

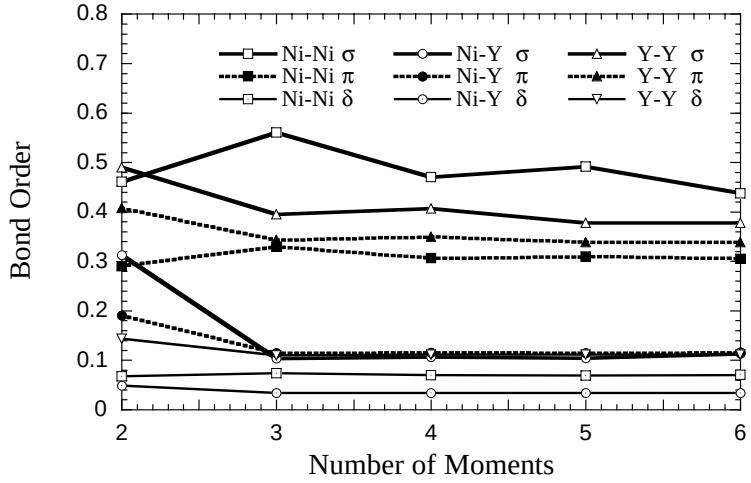

Figure 2.1 Dependence of the bond order for the bondings in the bulk structure to the number of moment.

Table 2.2 Bond order for covalent d-d interactions in Ni_2Y phase within angular dependent second moment approximation.

	σ	π	δ
Θ_{NiNi}	0.4612	0.2906	0.0672
Θ_{NiY}	0.3131	0.1908	0.0488
Θ_{YY}	0.4901	0.4074	0.1434

N_{d} in the above expressions is derived using the rectangular band model for d bands [13] and N_{s} is derived regarding rest of the valence electrons as sp valence electrons. Local charge neutrality is imposed upon each Ni and Y atoms and the site-diagonal energy shift is calculated within tight-binding-Hartree-Fock approximation following reference [5];

$$\Delta N_{\mathrm{s},\alpha} + \Delta N_{\mathrm{d},\alpha} = 0, \quad (\alpha = \text{Ni, Y}) \tag{2.6}$$

$$x_{\mathrm{Ni}}\Delta N_{\mathrm{d,Ni}} + x_{\mathrm{Y}}\Delta N_{\mathrm{d,Y}} = 0 \tag{2.7}$$

$$\Delta E_\alpha = u_{\mathrm{dd}}\Delta N_{\mathrm{d},\alpha} + u_{\mathrm{sd}}\Delta N_{\mathrm{s},\alpha} + V\sigma Z(\Delta N_{\mathrm{d},\alpha} + \Delta N_{\mathrm{s},\alpha}). \tag{2.8}$$

$\Delta N_{\rm s}$ and $\Delta N_{\rm d}$ are the shift of the number of s and d valence electrons from arbitrary initial values. In this calculation, $N_{\rm s,Ni} = 1.40, N_{\rm d,Ni} = 8.60, N_{\rm s,Y} = 1.31, N_{\rm d,Y} = 1.69$ for pure Ni and Y [5] are used as initial values, and $u_{\rm dd} = 1.6{\rm eV}, u_{\rm sd} = 0.75{\rm eV}, V = 0.25{\rm eV}$ are used [14]. x_α is the concentration of α atom. $\Delta N_{\rm s}$ and $\Delta N_{\rm d}$ are determined such that equations from (2) to (4) are self-consistent. The final values for Ni and Y in Ni_2Y phase are as follows; $N_{\rm s,Ni} = 1.65, N_{\rm d,Ni} = 8.35, N_{\rm s,Y} = 0.81, N_{\rm d,Y} = 2.19$.

For the calculations for Ni-Y interaction, $\sqrt{N_{\rm Ni}N_{\rm Y}}$ is used instead of N_α where needed.

Figure 2.2 shows the total hybridized NFE-TBB effective interatomic potentials given by equation 2.1.

2.2.2 Molecular dynamics calculation

The constant temperature Nosé-Hoover equations of motion are used for the present molecular dynamics calculations, [15, 16];

$$m_i \dot{\boldsymbol{v}}_i = \boldsymbol{F}_i - \zeta m_i \boldsymbol{v}_i \tag{2.9}$$

$$\dot{\zeta} = 2(K - K_0)/Q, \tag{2.10}$$

where K is the kinetic energy of the system and K_0 is the kinetic energy corresponding to the desired temperature. The temperature is set to 773K throughout the present study.

The molecular dynamics simulations for this chapter have the following initial conditions:

- Perfect crystal;
- Crystal structure with vacancy;
- Crystal structure with grain-boundary;

Details of each condition is presented in the corresponding subsection in the section 2.3.

For all conditions, Q is set to 1.000×10^9 (atomic unit) except for the grain-boundary conditions, $Q = 1.189 \times 10^5$ (atomic unit). Determined Q is such that the fluctuations of the total kinetic and potential energy are small, not to violate the crystal structure by a sudden jump of the temperature of the simulated system. As a result, the peaks in the radial distribution functions for the reference crystal

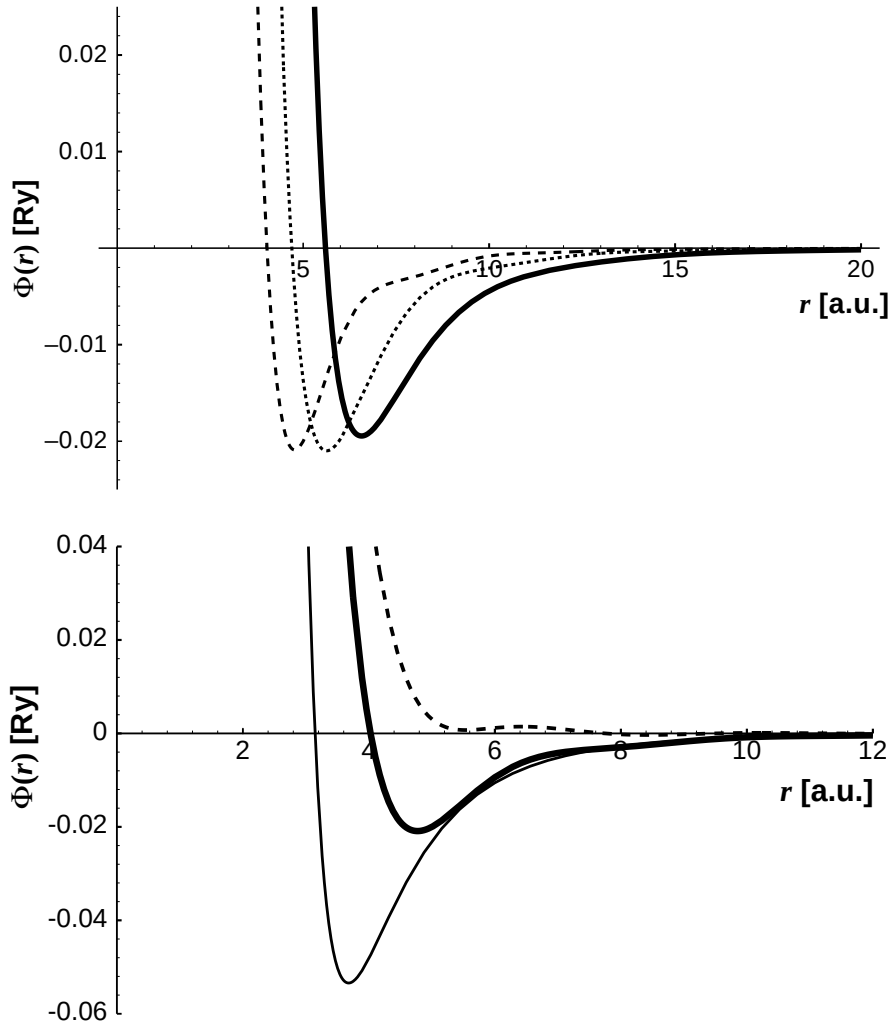

Figure 2.2 Effective interatomic potential for Ni-Ni, Ni-Y and Y-Y interactions (upper panel). The dashed line is for Ni-Ni interaction, the dotted line is for Ni-Y interaction and the solid line is for Y-Y interaction. Interatomic potential for sp and d interactions for Ni-Ni (lower panel). The dashed line is for sp interaction, the thin solid line is for d interaction and the bold solid line is for total interaction.

structure is reproduced. The adopted values are much larger than those characterized by Holian *et al.* [17]. Therefore, for conditions other than the grain-boundary condition, the systems are weakly-coupled, although for the grain-boundary condition, the simulated system is coupled to the thermostat with the response time corresponding to the Einstein frequency.

For the calculation of the self-diffusion coefficient, Einstein relation for the diffusion coefficient [18] is used;

$$D = \lim_{t\to\infty} \langle |\boldsymbol{r}(t) - \boldsymbol{r}(0)| \rangle / 6t. \tag{2.11}$$

Self-diffusion coefficients are evaluated from mean square displacement plots against time.

The autocorrelation function and the spectral density of velocity $\boldsymbol{v}(t)$ are [18];

$$C(t) = \langle \boldsymbol{v}(t) \cdot \boldsymbol{v}(0) \rangle \tag{2.12}$$

$$I(\omega) = 2\int_0^\infty C(t) \cos \omega t \, dt. \tag{2.13}$$

2.3 Results and discussions

2.3.1 Perfect crystal calculation

For the initial configuration, $3 \times 3 \times 3$ crystallographic unit cells i.e. 432 Ni atoms and 216 Y atoms are set in the simulation supercell. Bond order is calculated applying equation 2.5 to the initial reference crystallographic structure. Many-body attractive force is then replaced by the sum of pairwise attractive force. Equations of motions are integrated numerically with leap-frog method [19] over $10\,000$ steps after $5\,000$ equilibration steps with $\Delta t = 1.0 \times 10^{-15}$ s and the force calculation is cut off at 7.181Å, which is the same as the lattice constant for Ni_2Y.

Figure 2.3 shows the radial distribution function for Ni-Ni at 773K. Sharp peaks show that the perfect crystal structure for Ni_2Y is well reproduced by molecular dynamics. Mean square displacements are given in figure 2.4 and spectral density of velocity is given in figure 2.5. No diffusive motion is observed and very small number of vibrational modes are visible. The frequencies of the modes clearly visible are almost the same for both Ni and Y.

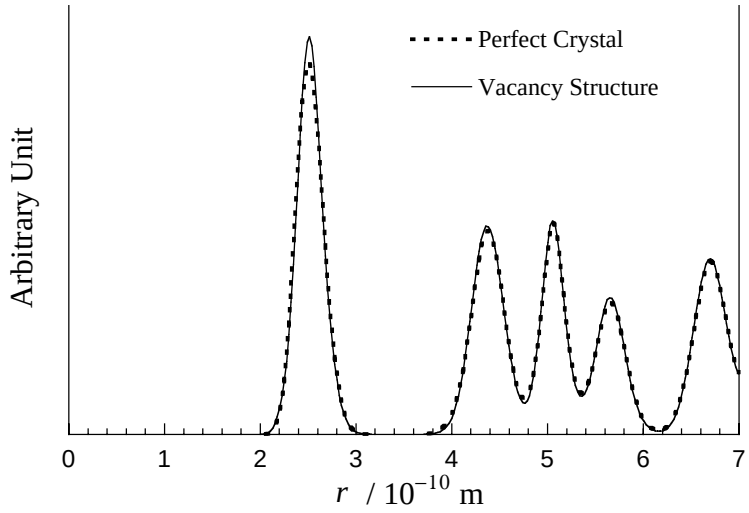

Figure 2.3 Radial distribution functions for Ni-Ni at 773K. The dashed line shows the distribution in the perfect crystal and the solid line shows the distribution in the Ni vacancy structure.

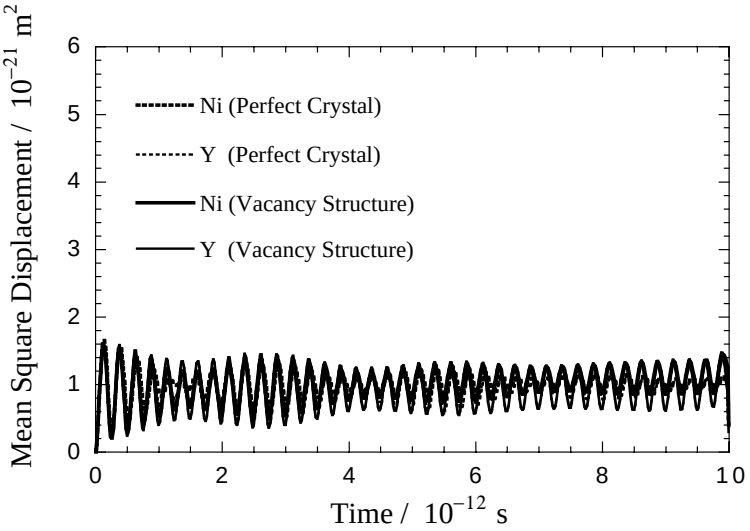

Figure 2.4 Mean square displacements (MSD) at 773K. The dashed line shows the MSD in a perfect crystal and the solid line shows the MSD in a Ni vacancy structure. The bold lines represent Ni and the thin lines represent Y.

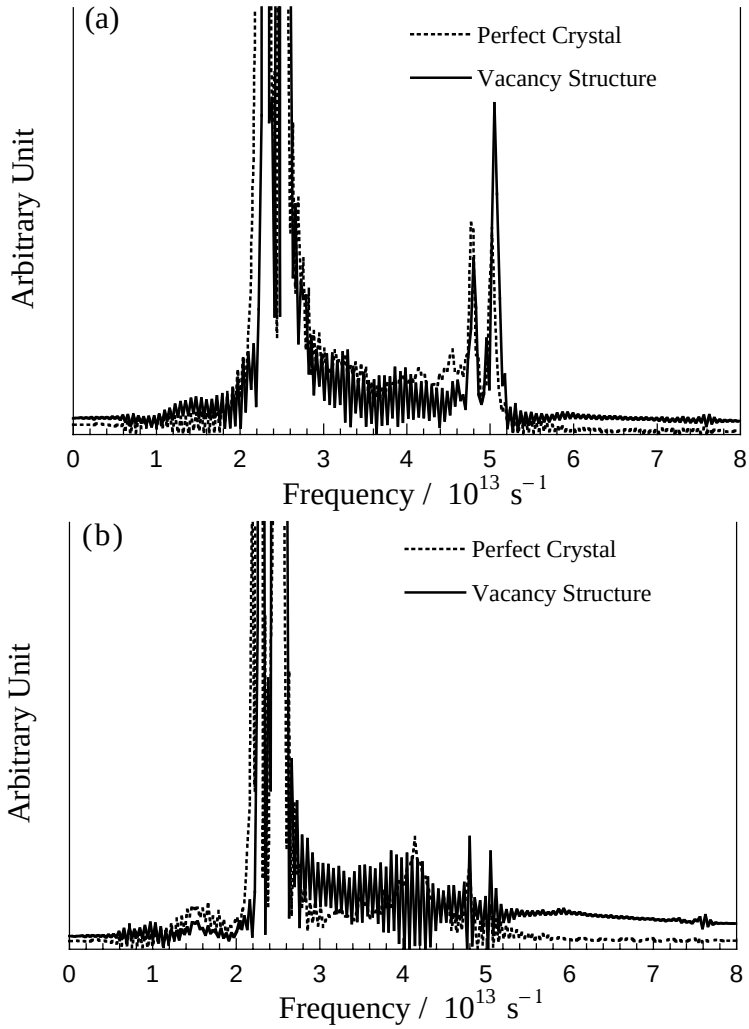

Figure 2.5 Spectral densities of velocity for (*a*) Ni and (*b*) Y at 773K. The dashed line is for a perfect crystal and the solid line is for a Ni vacancy structure.

2.3.2 Vacancy structure calculation

The structures same as presented in section 2.3.1 with a Ni vacancy and two Ni vacancies in the unit cell at the centre are adopted, as the two initial configurations for vacancy structure simulations. The choice of Ni vacancy is due to the results of the estimation of the vacancy formation energy that show the formation energy for Ni vacancy is half as small as those for Y vacancy (See appendix B). The numerical conditions are the same as section 2.3.1 for both, except the number of steps, which is $18\,000$ for the two-vacancies structure.

The radial distribution function for Ni-Ni pair at 773K for the one-vacancy condition is shown in figure 2.3. Compared with the perfect crystal structure, there are almost no differences observed in all of the Ni-Ni, Ni-Y and Y-Y distribution curves. The reference crystallographic Ni_2Y structure is also well reproduced in the vacancy structure simulation. Mean square displacements are given in figure 2.4 for one vacancy condition and again no diffusive motion is observed. This is also the case for two-vacancies condition. Spectral density curves are given in figure 2.5 and figure 2.6. Both the one-vacancy and the two-vacancies structures have a similar sharp peaks structure but the frequency of the main peaks are shifted from that of the perfect crystal in the two-vacancies condition. Again, no diffusive mode is observed for two conditions.

Direct many-body attractive force calculation by equation 2.5 is also performed for one Ni vacancy initial condition over $7\,000$ time steps. Conditions for this simulation is the same as in the pairwise force calculation. No diffusive motions are observed again both in the mean square displacements and in the spectral densities. An example of the atomic motions near Ni vacancy are shown in figure 2.7. Both Ni and Y atoms fluctuates around their initial atomic position and no jump motion is observed. Initial regular atomic arrangements is conserved even for the atoms neighbouring the vacancy.

2.3.3 Grain-boundary structure calculation

In order to take the effect of the grain-boundary into account, a symmetric tilt boundary model containing $1\,080$ (720 Ni and 360 Y) atoms with $\theta = 0.321\,8$ rad is used for initial configuration. For initial coordinates, atoms are arranged as shown in figure 2.8. The cell contains 432 (288 Ni and 144 Y) fixed atoms.

The computational conditions for this calculation are different in order to achieve faster computation per atom. This is because more atoms are set in the simulation unit cell and many-atom attractive force calculation is used for

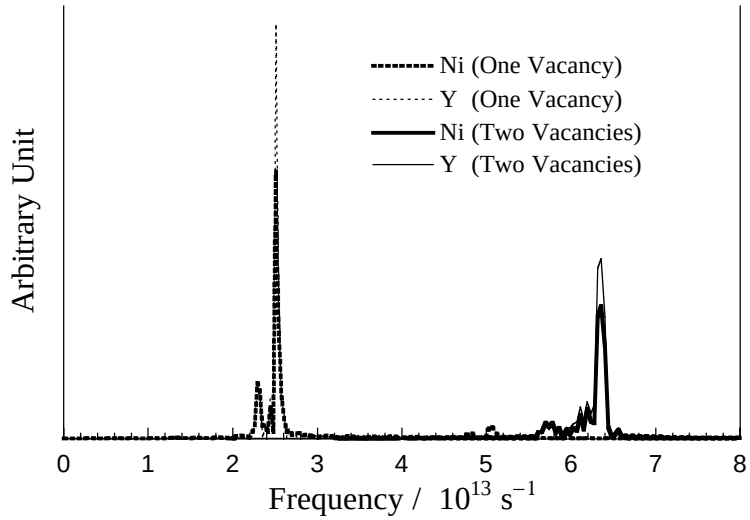

Figure 2.6 Spectral densities of velocity for Ni and Y at 773K. The dashed line is for a one-vacancy structure shown in figure 2.5 and the solid line is for a two-vacancies structure. The bold lines represent Ni and the thin lines represent Y.

anisotropic and inhomogeneous atomic arrangements. The equations of motions are integrated with Størmer algorithm [20] over $10\,000$ time steps after $5\,000$ equilibration steps with $\Delta t = 1.0 \times 10^{-15}$ s. Force cut off lengths are set to 5.027Å for Ni-Ni, 5.821Å for Ni-Y and 6.350Å for Y-Y (9.500, 11.00 and 12.00 in atomic unit respectively).

Data analysis in this condition is done using 100 sample coordinates out of $10\,000$ time steps coordinates chosen at every 100th steps. Figure 2.9 shows the horizontal and vertical mean square displacements in the following definitions of the corresponding diffusion coefficients;

$$D_{x^2+y^2} = \lim_{t\to\infty} \langle |x(t) - x(0)|^2 + |y(t) - y(0)|^2 \rangle / 4t \qquad (2.14)$$

$$D_{z^2} = \lim_{t\to\infty} \langle |z(t) - z(0)|^2 \rangle / 2t \qquad (2.15)$$

$D_{x^2+y^2}$, which characterizes the diffusivity of the horizontal motion in the plane parallel to the grain-boundary, is the self-diffusion coefficient calculated from horizontal mean square displacement and D_{z^2}, which characterizes the diffusivity of the vertical motion to the grain-boundary plane, is the self-diffusion coefficient calculated from vertical mean square displacement, for grain-boundary is $z = 0$. Both horizontal and vertical mean square displacements increase monotonously

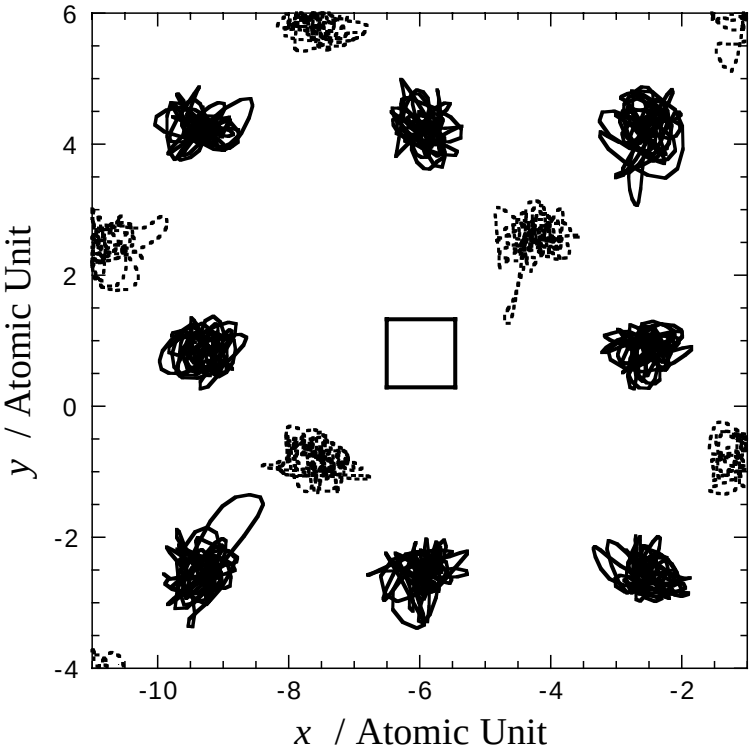

Figure 2.7 Examples of the atomic motions near Ni vacancy projected onto a two dimensional plane. The solid lines show Ni trajectories and the dashed lines show Y trajectories. Open square represents a Ni vacancy.

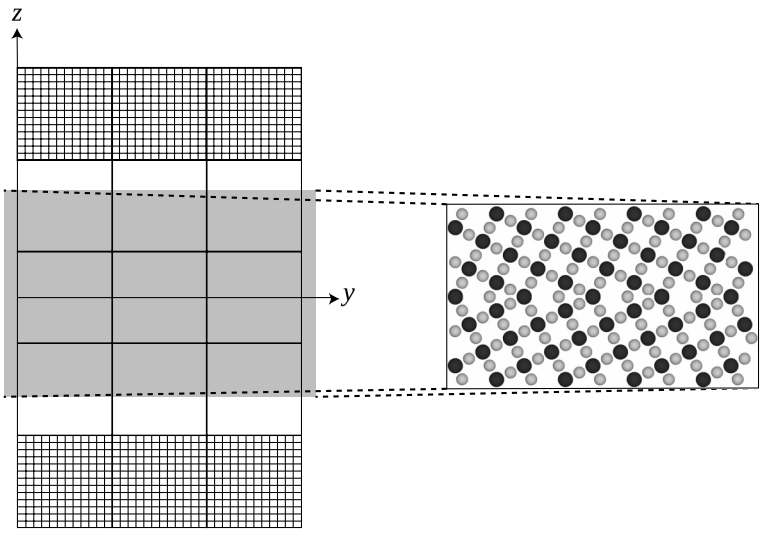

Figure 2.8 The model for molecular dynamics simulation for a grain-boundary structure in Ni_2Y phase. The schematic of the computational cell and the projected atomic arrangements. The periodic boundary conditions are posed on all borders except on the z borders. Meshed regions correspond fixed atoms.

with time and therefore diffusive motion can be clearly observed. Calculated self-diffusion coefficients are $D_{x^2+y^2} = 6.695 \times 10^{-11}$ m^{2}s^{-1} and $D_{z^2} = 7.349 \times 10^{-11}$ m^{2}s^{-1} for Ni and $D_{x^2+y^2} = 2.902 \times 10^{-10}$ m^{2}s^{-1} and $D_{z^2} = 3.028 \times 10^{-10}$ m^{2}s^{-1} for Y. Against expectation, the horizontal and the vertical mean square displacements does not differ from each other. The possible reason for this is that the high rate diffusion does occur in the grain-boundary region, but that the range that enables large diffusivity is wider than expected.

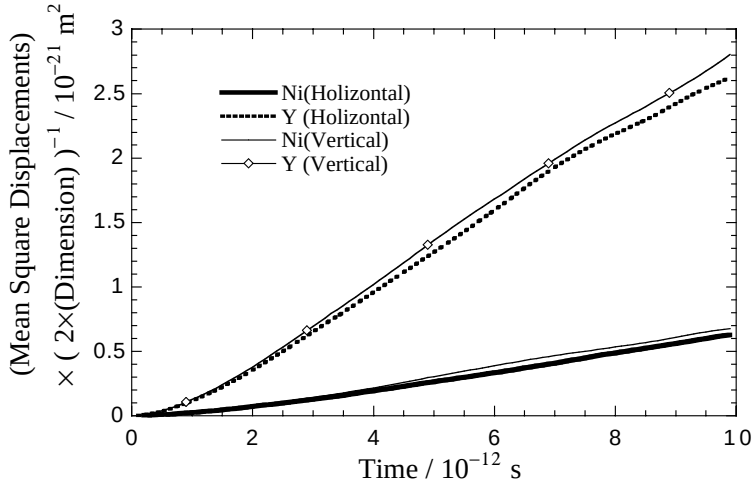

Figure 2.9 Mean square displacements (MSD) at 773K. The solid line shows a horizontal MSD in the Ni, the dashed line shows a horizontal MSD for Y, thin line shows a vertical MSD for Ni and thin line with open square markers shows a vertical MSD for Y.

Additional $3\,000$ time steps calculation with higher sampling rates of coordinates is performed for two reasons; to see the atomic arrangements after sufficiently long time steps through radial distribution function, and to calculate the spectral densities of velocity with sufficiently good precision.

Figure 2.10 shows the radial distribution function for grain-boundary structure calculated for the additional $3\,000$ time steps. The obtained curves are not so smooth as those in figure 2.3, but sharp peaks structure can be observed for all distributions except for Y-Y pair distribution. The distribution function for Y-Y shows the structure of Y is disordered although we adopted larger $r_{\rm cut}$ than those for other two types of interactions. Most of the peaks observed are the same as those observed for the perfect crystal structure, but one extra peak is visible for

each distribution in the short range. For the perfect crystal structure, such short interatomic separations are unfavourable because of the strong repulsive interactions (see figure 2.2). This one extra peak is also observed for the preceding $10\,000$ time steps simulation. This may be the one for the relaxed short separations set in the initial configuration. As we see, they are not vanished even after 10ps, which is characteristic for the atomic jump calculated with figure 2.9 and the crystallographic separations. This short interatomic separations can be possible probably because we have used the direct many-body attractive force calculation.

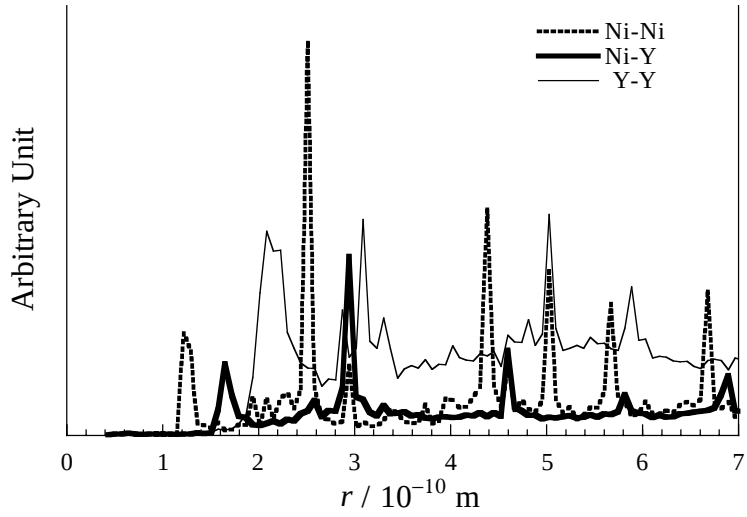

Figure 2.10 Radial distribution function for the grain-boundary structure at 773K calculated from $1/10$ sample coordinates in additional $3\,000$ time steps simulation. The dashed line shows Ni-Ni pair distribution, the bold solid line shows Ni-Y pair distribution and the thin solid line shows Y-Y pair distribution.

The diffusive motion is also observed as the zero frequency mode in the spectral densities shown in figure 2.11.

Presented in figure 2.12 are the plots of the self-diffusion coefficients of both horizontal and vertical motions. It proves that the rate of the self-diffusion becomes higher when atoms are near the grain-boundary but the values themselves remain high throughout the simulation cell size used in this model.

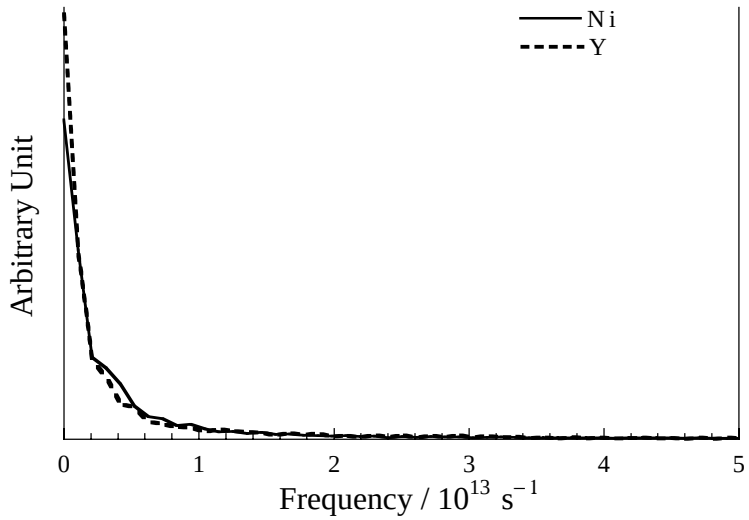

Figure 2.11 Spectral densities of velocity for Ni and Y at 773K in the grain-boundary structure calculated from $1/10$ sample velocities in additional $3\,000$ time steps simulation. The solid line is for Ni and the dashed line is for Y.

2.4 Conclusions

A molecular dynamics simulation on Ni_2Y intermetallic phase has been done with a hybridized nearly-free-electron–tight-binding-bond interatomic interaction model.

Ordered structure was reproduced for the several structure models for this intermetallic phase.

High rate self-diffusion phenomena has only been observed in the symmetrical grain-boundary model among three structure models, and the conclusion is that the high growth rate of Ni_2Y phase accomplished in the electrochemical experiments is due to the high diffusion rate in and near the grain-boundaries.

The dynamical structure of Ni vacancy structure model made no significant difference from a perfect crystal structure model. Therefore, it is difficult to ascribe the cause of the high growth rate to the standard vacancy model of diffusion.

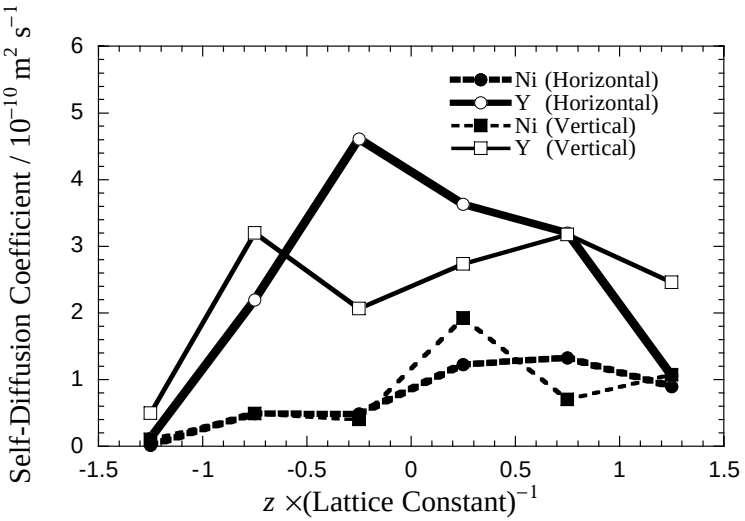

Figure 2.12 Variation of the horizontal and the vertical self-diffusion coefficients versus z axis neutral to grain-boundary. The bold lines represent the horizontal self-diffusion coefficients and the thin lines represent the vertical self-diffusion coefficients. For both two coefficients, dashed lines represent Ni and the solid lines represent Y.

References

[1] G. Xie, K. Ema and Y. Ito, *J. Appl. Electrochem.* **24** 321 (1994).

[2] P. Egelstaff, *An Introduction to the Liquid State* (Academic Press, London, 1967).

[3] P. G. Shewmon, *Diffusion in Solids* (McGraw-Hill, New York, 1963).

[4] D. G. Pettifor, *Bonding and Structure of Molecules and Solids* (Oxford University Press, Oxford, 1995).

[5] Ch. Hausleitner and J. Hafner, *Phys. Rev.* B**45** 115 (1992).

[6] D. G. Pettifor and M. A. Ward, *Solid State Commun.* **49** 291 (1984).

[7] N. W. Ashcroft, *Phys. Lett.* **23** 48 (1966).

[8] A. P. Sutton, M. W. Finnis, D. G. Pettifor and Y. Ohta, *J. Phys. C: Solid State Phys.* **21** 35 (1988).

[9] J. M. Wills and W. A. Harrison, *Phys. Rev.* B**28** 4363 (1983).

[10] H. Yamada, J. Inoue, K. Terao, S. Kanda and M. Shimizu, *J. Phys. F: Met. Phys.* **14** 1943 (1984).

[11] D. G. Pettifor and M. Aoki, *Philos. Trans. R. Soc. London* Ser. A **334** 439 (1991).

[12] D. G. Pettifor, *Many-Atom Interactions in Solids*, edited by R M Nieminen, M J Puska and M J Manninen (Springer-Verlag, Berlin, 1990) p 64.

[13] W. A. Harrison, *Electronic Structure and the Properties of Solids* (Freeman, San Francisco, 1980) .

[14] D. Nguyen-Manh, D. Mayou, A. Pasturel and F. Cyrot-Lackmann, *J. Phys. F: Met. Phys.* **15** 1911 (1985).

[15] S. Nosé, *J. Chem. Phys.* **81** 511 (1984); *Mol. Phys.* **52** 255 (1984).

[16] W. G. Hoover, *Phys. Rev.* A**31** 1695 (1985).

[17] B. L. Holian, A. F. Voter and R. Ravelo, *Phys. Rev.* E**52** 2338 (1995).

[18] D. A. McQuarrie, *Statistical Mechanics* (Harper and Row, New York, 1976).

[19] M. P. Allen and D. J. Tildesley, *Computer Simulation of Liquids* (Oxford University Press, Oxford, 1987).

[20] W. G. Hoover, *Computational Statistical Mechanics* (Elsevier, Amsterdam, 1991).

Chapter 3

Hybridized NFE-TBB model of the bonding in the light-actinide metals

3.1 Introduction

The transport properties in the light-actinide metals and their compounds have been one of the most important problems in the energy conversion process. To study their detailed diffusional mechanism from the atomistic point of view, we must very often use a theoretical method such as molecular dynamics simulation. For the application of the molecular dynamics simulation to these problems, the dynamic structure of a system must be simulated over considerably long time steps and therefore the interatomic potentials used must be computationally efficient as well as physically appropriate for these materials.

In the last few decades, several interatomic potential models for the light-actinide metals have been developed.

Harrison [1] proposed a hybridized nearly-free-electron–tight-binding-bond (NFE-TBB) model of the very simple two-body potential based on the two-fluid model [2] and found that it can successfully predict the trends in the equilibrium spacings and the bulk moduli of the light-actinide metals qualitatively.

This model was extended to be more realistic for the calculation of the phonon spectra and the elastic constants of α-Th at the cost of its simplicity [3].

Chen [4] developed a more efficient model using the local volume potential (LVP), which is related to the embedded atom method (EAM) [5]. Their estimation of the elastic constants for α-Th using LVP was shown to give a very good agreement with the experimental data.

Although the hybridized NFE-TBB model by Harrison has a physically transparent formulation and the LVP is a very efficient formulation for parameter fitting, they usually need to include at least a few nearest-neighbours interaction to reach a good agreement with the experimental value. To achieve a good agreement with the experimental data by including long-range interactions may not always be physical. Moreover, while the structures of the light-actinide elements are said to be strongly affected by the complex spatial shape of the f spherical harmonics, these models do not contain any directional character of the bonding.

Motivated by these facts, the aim of the present chapter is set as to demonstrate how we can achieve a good agreement of the calculated elastic constants with the experimental data by using angular-dependent short-range potential, not by using long-range pairwise potential.

The hybridized NFE-TBB model for the description of the bondings in the light-actinide metals is used but designed to model these metals through first-nearest-neighbour interaction model by including a simplified bond-angle dependence and by adjusting the tight-binding parameters.

The choice of the formulation for the hybridized NFE-TBB model corresponds to that of Hausleitner and Hafner [6] for the transition-metal alloys. The points new or different in this chapter are as follows; (1) Analytical expression [7] is used for the NFE part, (2) TBB part is changed for the f-electron systems corresponding to the f-f transfer integral and (3) expression for the bond order in the first-nearest-neighbour bond order potential [8] is adopted for the bonding interactions instead of the one using the Bethe lattice method. As a result of the last point, the bonding interaction depends on the structure directly.

This choice of the formulation results in a non-pairwise first-nearest-neighbour effective interaction potential determined by the arrangement of the atoms up to the second-nearest-neighbour shell of an atom.

Unfortunately, this model is not enough to give the correct energy difference between fcc and hcp structures, because there is no way to differentiate energies between these two structures only by their first- or second-nearest-neighbour structures. But I have examined how this model can reproduce the experimental elastic constants, and confirmed that this model can give, at least, the correct energy change against the atomic displacement near equilibrium.

In section 3.2, the method for the first-nearest-neighbour potential for the f-electron system is outlined. Then, this potential is applied to fcc Th and Pu and the results of the calculation of the elastic constants are given and then compared with the experimental values in section 3.3. In section 3.4, conclusions for this chapter are presented.

3.2 Computational method

The hybridized NFE-TBB model of the interatomic potential is as follows:

$$\Phi_{\mathrm{total}} = \Phi_{\mathrm{NFE}} + \Phi_{\mathrm{TB,rep}} + \Phi_{\mathrm{TB,bond}}. \tag{3.1}$$

The first term treats the spd-electron gas as an sp-electron gas in simple metal. The remaining terms are for the TBB part of the potential for the f-electron, but the second term for the pairwise repulsive interaction differs from the standard tight-binding model [1].

The following NFE interaction formulation by Pettifor and Ward [7] is adopted;

$$\Phi_{\mathrm{NFE}} = \frac{2N_{\mathrm{s},i}N_{\mathrm{s},j}}{r_{ij}} \sum_{n=1}^{3} A_n \cos(k_n r + \alpha_n) \exp(\kappa_n r_{ij}). \tag{3.2}$$

$N_{\mathrm{s},i}$ is the number of spd-valence electrons for the i atom. This parameter is set as 3 for Pu and also for Th, as in the Harrison's study [1]. As in the model of Singh et al.[3], Heine-Abarenkov model potential is used to calculate the parameters A_n, α_n, k_n and κ_n [9] and all of them are determined by r_{c} and D.

The following is the repulsive interaction used;

$$\Phi_{\mathrm{TB,rep}} = \frac{\sqrt{N_{\mathrm{f},i}N_{\mathrm{f},j}}}{11} \frac{h_{ij}^2 d_{ij}^{14}}{r_{ij}^{12}}. \tag{3.3}$$

$N_{\mathrm{f},i}$ is the number of f-valence electrons for the i atom and is determined as the number of total valence electrons minus $N_{\mathrm{s},i}$. d_{ij} is the equilibrium interatomic separation. The interatomic matrix elements form by Harrison [1] is used and the all matrix elements and their average h are determined by a single parameter, r_{f}.

Bond energy expression is;

$$\Phi_{\mathrm{TB,bond}} = 2 \sum_{\alpha\beta} H_{j\beta,i\alpha} \Theta_{i\alpha,j\beta}. \tag{3.4}$$

$H_{j\beta,i\alpha}$ is the tight-binding Hamiltonian and $\Theta_{i\alpha,j\beta}$ is the bond order. Bond order is calculated from the following simplified expression [8], [10];

$$\Theta_{i,j}^{\alpha} = \widehat{\chi}(N_{\mathrm{f}}) \Bigg/ \left\{ 1 + \frac{1}{2} \sum_{k \neq i,j} \left[\left(\frac{h_\alpha(r_{ik})}{h_\alpha(r_{ij})} \right)^2 g_\alpha(\theta_{jik}) + \left(\frac{h_\alpha(r_{jk})}{h_\alpha(r_{ij})} \right)^2 g_\alpha(\theta_{ijk}) \right] \right\}^{1/2}. \tag{3.5}$$

The suffix α denotes σ, π, δ and ϕ and h_α corresponds to the interatomic element linking α orbital at each atom. $\widehat{\chi}(N_{\rm f})$ is the reduced susceptibility. $g(\theta)$ is an angularly dependent embedding function for each type of the bond.

Note that the sum for k is taken only for the atoms which are in the first-nearest-neighbours positions of the both i and j in this case.

The form for g as a function of bond angle θ is given in the same way as in the reference of Pettifor [11], but here, the table of matrix elements given by Sharma [12] is used instead of the Slater-Koster table [13] as the f-f matrix elements are treated now. The following form is derived for $g(\theta)$ and the coefficients for each α are compiled in table 3.1.

$$g_\alpha(\theta) = F_{0,\alpha} + F_{2,\alpha}\cos(2\theta) + F_{4,\alpha}\cos(4\theta) + F_{6,\alpha}\cos(6\theta). \tag{3.6}$$

The resulting $g(\theta)$ curves are shown in figure 3.1.

Table 3.1 Calculated coefficients for the angularly dependent embedding function.

α	F_0	F_2	F_4	F_6
σ	0.458594	0.352734	0.147656	0.041016
π	0.719028	0.233333	0.043750	−0.058333
δ	3.278646	−0.865885	−1.549479	0.136719
ϕ	94.515625	−117.304690	24.609375	−0.820313

The hybridized NFE-TBB potential used in this chapter is determined by three adjustable parameters, $r_{\rm c}$, D and $r_{\rm f}$. These parameters are set as the interatomic spacing d and the bulk modulus B to be reproduced.

The elastic constants are derived as follows. First, the change of the binding energy per atom U for a certain deformation of the lattice structure is assumed to be written as the sum of the change of the interatomic potential. Then, $C' = 1/2(C_{11} - C_{12})$ and C_{44} are given by the second derivative of the binding energy with appropriate deformations:

$$C_\lambda = \frac{1}{12\Omega}\frac{d^2U(\gamma_\lambda)}{d\gamma_\lambda^2} \quad (\lambda = 1, 2), \tag{3.7}$$

where $C_\lambda \quad (\lambda = 1, 2)$ correspond to C' and C_{44} and Ω is the atomic volume. The deformation γ_λ are taken as the strain matrix elements introduced in the literature [8]. The bulk modulus B is derived from

$$B = \Omega\left(\frac{d^2U}{d\Omega^2}\right)_{\Omega=\Omega_0}, \tag{3.8}$$

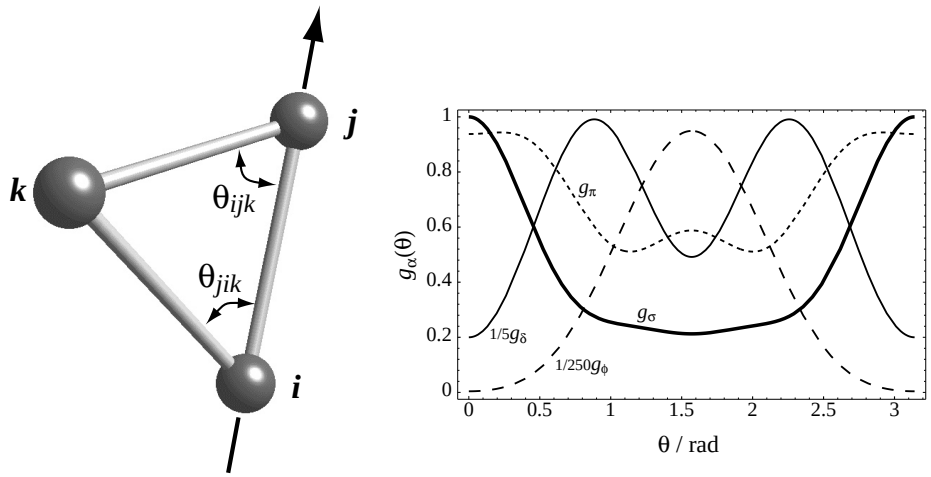

Figure 3.1 Schematic of the bonding (left panel) and the schematic of the bond angles and the angular dependence of the embedding function $g(\theta)$ (right panel).

where Ω_0 is the equilibrium atomic volume.

3.3 Results

3.3.1 Potentials for fcc Th

The fcc structure for Th is stable at room temperature. The experimental crystallographic structure of α-Th [14] is used for calculations. The data used for the lattice constant is $a = 5.0842$Å.

As this potential function has a non-pairwise interaction term in the TBB part, it is not trivial how to set the uniform cut off length $r_{\rm cut}$ between first and second nearest-neighbour distances. The cut off length for fcc Th is set as $r_{\rm cut} = 4.5195$Å (8.5406a.u.), which gives $\phi(r_{\rm cut}) = 0$ if we fix all variables r and θ in equation 3.5 and 3.6 to the interatomic separation and the bond angle of the non-strained crystallographic structure respectively. In this case, the potential ϕ results in a pairwise interaction.

The results of the fitting to the experimental data for d and B are compiled in table 3.2 and the adjusted parameters are as follows; $r_{\rm c} = 1.1472$Å, $D = 0.9109$ and $r_{\rm f} = 0.5766$Å. As the experimental data for d in table 3.2 has only two figures after decimal point, a calculated interatomic spacing $d = 3.5951$Å from the lattice

constant data [14] is used for the fitting.

The resulting interatomic potential calculated using these parameters is given in figure 3.2. The potential curve shown in figure 3.2 is derived with the bond orders for the bonding with the first-nearest-neighbour atom and it shows the angular-dependent non-pairwise potential describing first-nearest-neighbour bond direction and the angular-independent pairwise potential at the same time.

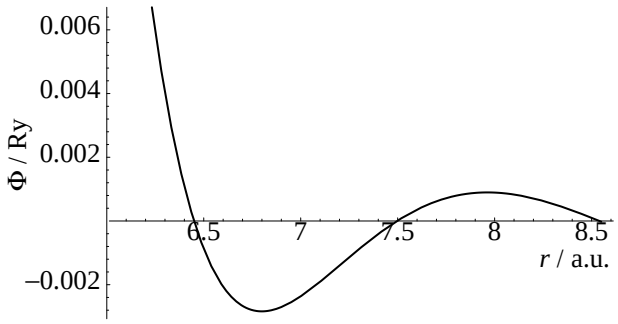

Figure 3.2 Interatomic potential for fcc Th at 0K. Potential energy curve toward first-nearest-neighbour bond direction.

A $U-\gamma$ curve calculated from this potential is given in figure 3.3. The second-order polynomial fit shown in the figure is obtained by a least-square fitting to the plotted binding energy.

The calculated elastic constants for α-Th at 0K are given in table 3.2. The Cauchy pressure $C_{12}-C_{44}$ for this crystal is calculated to be positive (2.64GPa) though negative for experimental 0K data (-0.15GPa). This negative Cauchy pressure is only observed at temperatures below 40K. At room temperature, Cauchy pressure is measured to be positive (5.34GPa, 300K) also for experimental data [15].

The elastic constants with the above mentioned pairwise potential have also been calculated. In this potential, the bond order for each type of bond becomes a constant and fixed to its value at the non-strained structure. Therefore it becomes to have a pairwise and angular-independent character. The pairwise and non-pairwise potentials are identical for the bonding direction from an atom at a equilibrium crystallographic structure. A same set of parameters is used as non-pairwise potential. By choosing same parameters, the same d and B are obtained because they depend only on r. The calculated elastic constants are also given in table 3.2.

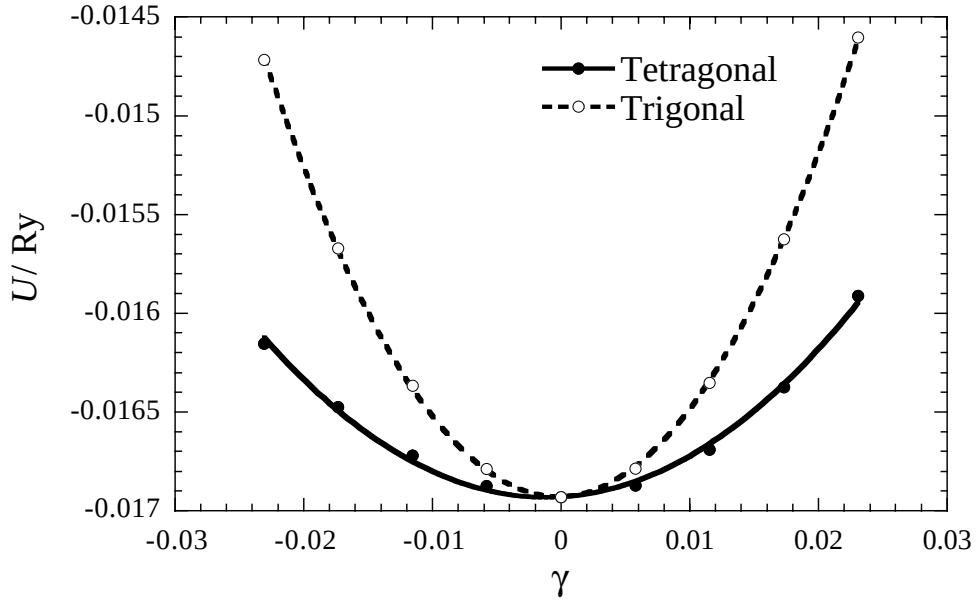

Figure 3.3 Binding energy per atom as function of γ for tetragonally and trigonally deformed fcc Th. The curves are second-order polynomial fits.

A better agreement of the calculated C' with the experimental data is enabled

Table 3.2 Calculated and experimentally determined elastic constants of α-Th at 0K. The elastic constants are listed in GPa. Calculated also are the elastic constants by a pairwise potential with fixed bond order. The parameters used are the same for two calculations.

	Calculated		Experimental
	non-pairwise	pairwise	
C_{11}	86.84	93.55	81.03^a
C_{12}	49.70	46.34	50.31^a
C_{44}	47.06	47.38	50.46^a
C'	18.57	23.61	15.36^b
B	62.08	62.08	60.55^b
d [Å]	3.5982	3.5982	3.60^c

a: Ref. [15], b: Calculated from C_{ij}, c: Ref. [16].

by including angular character. As is also the case for the sp-valent systems [8], we have found that the tetragonal shear is largely dependent on the angular character of the bondings.

3.3.2 Potentials for fcc Pu

The fcc structure for Pu is stable at elevated temperatures. This is called as δ-Pu and stable between 592K and 724K. The present hybridized NFE-TBB potential has also been tested for fcc structure of Pu with the lattice constant of δ-Pu, $a = 4.6371$Å at 713K [14], but we have done our calculations at 0K.

Cut off length is chosen as $r_{\rm cut} = 3.8943$Å (7.3592a.u.) in the same way as for fcc Th. The results of the fitting of d and B to the experimental data are compiled in table 3.3. The adjusted parameters are $r_{\rm c} = 0.9413$Å, $D = 0.7951$ and $r_{\rm f} = 0.4044$Å. The resulting potential energy curve is given in figure 3.4.

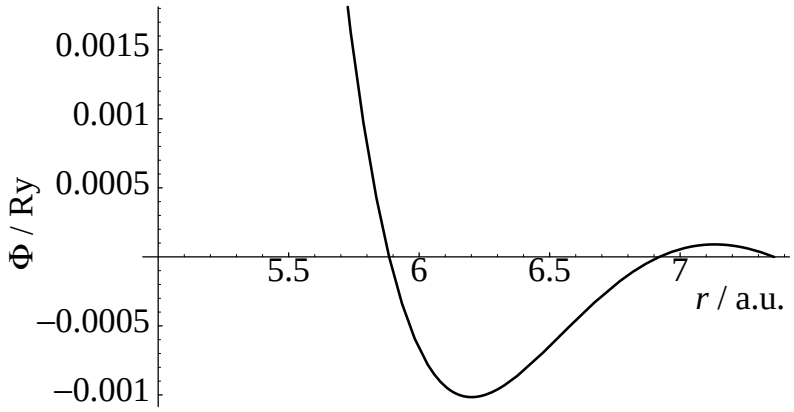

Figure 3.4 Interatomic potential for fcc Pu at 0K. Potential energy curve toward first-nearest-neighbour bond direction.

The calculated elastic constants using this potential is also given in table 3.3. The tabulated experimental elastic constants are those measured using a 1wt.% Ga-stabilized fcc Pu at room temperature [17]. Our choice of parameters reproduces both B and C' very well, therefore it reproduces C_{11} and C_{12} very well, but it does not reproduces unusually large value of the experimental C_{44} for this phase.

Table 3.3 Calculated and experimentally determined elastic constants of fcc Pu at room temperature. The elastic constants are listed in GPa. Calculated also are the elastic constants by a pairwise potential with fixed bond order. The parameters used are the same for two calculations.

	Calculated		Experimental
	non-pairwise	pairwise	
C_{11}	34.90	44.11	36.28^a
C_{12}	26.47	21.86	26.73^a
C_{44}	21.87	22.32	33.59^a
C'	4.21	11.13	4.78^a
B	29.28	29.28	29.91^a
d [Å]	3.2814	3.2814	3.2772^b

a: Ref. [17], b: Calculated from lattice constant in ref. [14].

Compared with the pairwise potential data, the agreement of the calculated C' with the experimental data has greatly improved as is also the case for fcc Th. The present model yield positive C' for fcc Pu, which means that this phase is stable towards a tetragonal shear. On the other hand, the first-principles calculation by Söderlind et al. [18] yields negative C', which means that this phase is unstable towards a tetragonal shear. They suggest that this phase is (and other high-temperature phases of U, Np and Pu are) stabilized by a thermal contribution to the energy, but I believe that C' for 0K must be also positive, because the temperature-dependence of the interatomic interactions are only comes into expression as a damping factor, $\exp(-\pi Tr/v_{\mathrm{F}})$ [19], where v_{F} is the Fermi velocity, and the sign of the C' is not changed. As for C_{44}, however, no improvement is observed. This may be because the experimental data are those of Ga-stabilized alloy, or because the present calculation is done for 0K and the sign of the Cauchy pressure has been changed as is also the case for fcc Th, or because our choice of the formula for the angular-dependence of the bonding is still too simplified.

3.4 Conclusions

Presented in this chapter is a first-nearest-neighbour hybridized nearly-free-electron–tight-binding-bond interatomic potential model for the light-actinide metals. Parameters in both NFE and TBB potential are adjusted to reproduce the experimentally known elastic constants for the fcc Th and Pu phase. In the present

scheme for deriving potential energy curves, some effects not included explicitly in the model, say, further-nearest-neighbour interactions or relativistic effects, are absorbed in the fitting parameters.

The results of the fitting to the bulk modulus and the equilibrium interatomic separation is good for both fcc Th and Pu. The derived potential with parameters adjusted by this fitting has shown very good agreement with the experimental data for the all three elastic constants for the cubic Th. The same procedure for fitting gives a very good agreement of the tetragonal shear constant C' and therefore good agreement of C_{11} and C_{12} with experimental data also for fcc Pu, but does not give good result for the trigonal shear constant C_{44}.

Angular-character of the bonding has greatly improved the reproducibility of the tetragonal shear constant C' compared with the angular-independent calculation. I have proved that by including angular-character of the bonding, we can describe at least the energy change against the fundamental shear strains for the cubic crystal structure even within first-nearest neighbour model of the bonding for the fcc light-actinide metals.

For the application of this model to the more complex structures of the light-actinides stable at room temperature, we may have to include higher moment terms in the calculation of the bond order.

References

[1] W. A. Harrison, *Phys. Rev.* **B**28, 550 (1983).

[2] M. S. S. Brooks, B. Johansson, and H. L. Skriver, in *Handbook on the Physics and Chemistry of the Actinides, Vol. 1*, edited by A. J. Freeman and G. H. Lander (North-Holland, Amsterdam, 1984), p. 153.

[3] N. Singh, and S. P. Singh, *Phys. Rev.* **B**42, 1652 (1990).

[4] S. P. Chen, *J. Alloys Compounds* **185**, 353 (1992).

[5] M. S. Daw and M. I. Baskes, *Phys. Rev.* **B**29, 6443 (1984).

[6] Ch. Hausleitner and J. Hafner, *Phys. Rev.* **B**45, 115 (1992).

[7] D. G. Pettifor and M. A. Ward, *Solid State Commun.* **49**, 291 (1984).

[8] P. Alinaghian, S. R. Nishitani and D. G. Pettifor, *Phil. Mag.* **B**69, 889 (1994).

[9] N. Singh, N. S. Banger and S. P. Singh, *Phys. Rev.* **B**39, 3097 (1989).

[10] S. R. Nishitani, P. Alinaghian, C. Hausleitner and D. G. Pettifor, *Phil. Mag. Lett.* **69**, 177 (1994).

[11] D. G. Pettifor, *Many-Atom Interactions in Solids*, edited by R. M. Nieminen, M. J. Puska and M. J. Manninen (Springer-Verlag, Berlin, 1990) p 64.

[12] R. R. Sharma, *Phys. Rev* **B**19, 2813 (1979).

[13] J. C. Slater and G. F. Koster, *Phys. Rev.* **94**, 1498 (1954).

[14] P. Villars and L. D. Calvert, *Pearson's Handbook of Crystallographic Data for Intermetallic Phases, 2nd ed.* (ASM International, Materials Park, 1991).

[15] J. D. Greiner, D. T. Peterson and J. F. Smith, *J. Appl. Phys.* **48**, 3357 (1977).

[16] C. Kittel, *Introduction to Solid State Physics, 7th ed.* (Wiley, New York, 1996).

[17] H. M. Ledbetter and R. L. Moment, *Acta Metall.* **24**, 891 (1976).

[18] P. Söderlind, O. Eriksson, J. M. Wills and A. M. Boring, *Phys. Rev.* **B**48, 9306 (1993).

[19] K. Takanaka and R. Yamamoto, *Phys. Stat. Sol.* (b) **84**, 813 (1977).

Chapter 4

Hybridized NFE-TBB model of the bonding in the aluminium metals

4.1 Introduction

The Al metal is known for its relatively low value of Young's modulus compared with Ti, Fe or Ni for example, which are known as the structural materials. Its alloys also can be used as light and highly elastic materials, such as Al-Li alloys, which are considered to be suitable for the aircraft structure material for saving fuel expenses. Studies of the dynamic structures of these materials must provide much useful knowledge for understanding or optimizing formation processes of these alloys.

For decades, molecular dynamics simulation is used for the detailed investigation of the atomistic process of the diffusion or the sputtering, which are essential for the investigations of the alloy formation or the investigations of the phenomena which largely determine the mechanical properties, such as the dynamic structures of the defects or the dislocations. To simulate dynamical properties by an atomistic simulation, it is essential to use both physically proper and efficient model of the interatomic potentials for the calculations of the interatomic forces to treat sufficiently long time scale for a system.

In this chapter, an hybridized NFE-TBB model of the potential have been examined for pure Al metal, a combination of the pairwise interaction potential for the NFE-like sp-electrons and the non-pairwise many-atom interaction potential for the d-electrons. The major advantages of the present model are that it accounts for the local structure more explicitly compared with the original hybridized NFE-

TBB model of the potential [1, 2] and that it is less complicated compared with the full many-atom calculation of the bonding interactions in the bond order potential [3] at the long-range interaction region which corresponds to the higher moment levels of the bond order potential. The former advantage is enabled because the present TBB part of the potential is characterized by the angular-dependent second-moment approximation of the bond order [4] instead of the one calculated with the Bethe lattice [2] or only with the coordination number [1], and the latter is because the present hybridized NFE-TBB potential is just a pairwise potential in that region.

As stated above, the bondings in the Al metal is treated as the coupling of the free-electron-like interactions due to the sp-electrons and the tight-binding interactions due to the d-electrons. That is, the d contribution to the bonding is not neglected. The inclusion of the d-state contributions, combined with the inclusion of its dependence on the bond angles, leads to the good agreement of the calculated elastic constants with the experimental data as we see later on.

In section 4.2, the choice of the potential model and the computational procedure for the fitting of its adjustable parameters are described, and the derivation of the data to be compared with the experimental ones is also described. The calculated data are given in section 4.3. Conclusions are also described in section 4.4.

4.2 Potential model and computational method

The hybridized NFE-TBB model of the interatomic potential is as follows:

$$\Phi_{\rm total} = \Phi_{\rm NFE} + \Phi_{\rm TB,rep} + \Phi_{\rm TB,bond}. \tag{4.1}$$

The first term treats the sp-electron gas in simple metal. The remaining terms are for the TBB part of the potential for the d-electrons.

The following NFE interaction formulation by Pettifor and Ward [5] is adopted;

$$\Phi_{\rm NFE} = \frac{2N_{\rm s}^2}{r_{ij}} \sum_{n=1}^{3} A_n \cos(k_n r + \alpha_n) \exp(\kappa_n r_{ij}). \tag{4.2}$$

$N_{\rm s}$ is the number of sp-valence electrons. Heine-Abarenkov model potential is used to calculate the parameters A_n, α_n, k_n and κ_n [6] and all of them are determined by $r_{\rm c}$ and D.

The following is the repulsive interaction used;

$$\Phi_{\rm TB,rep} = \frac{N_{\rm d}}{7} \frac{h_{ij}^2 d_{ij}^{10}}{r_{ij}^8}. \tag{4.3}$$

$N_{\rm d}$ is the number of d-valence electrons and is determined as the number of total valence electrons minus $N_{\rm s}$. d_{ij} is the equilibrium interatomic separation. The interatomic matrix elements form obtained by Wills and Harrison [1] is used and the all matrix elements and their average h are determined by a single parameter, $r_{\rm d}$.

Bond energy expression is;

$$\Phi_{\rm TB,bond} = 2\sum_{\alpha\beta} H_{j\beta,i\alpha}\Theta_{i\alpha,j\beta}. \tag{4.4}$$

$H_{j\beta,i\alpha}$ is the tight-binding Hamiltonian and $\Theta_{i\alpha,j\beta}$ is the bond order. Bond order is calculated from the following simplified expression [7];

$$\Theta^{\alpha}_{i,j} = \widehat{\chi}(N_{\rm d}) \Bigg/ \left\{ 1 + \frac{1}{2}\sum_{k\neq i,j} \left[\left(\frac{h_\alpha(r_{ik})}{h_\alpha(r_{ij})} \right)^2 g_\alpha(\theta_{jik}) + \left(\frac{h_\alpha(r_{jk})}{h_\alpha(r_{ij})} \right)^2 g_\alpha(\theta_{ijk}) \right] \right\}^{1/2}. \tag{4.5}$$

The suffix α denotes σ, π and δ orbitals, and h_α corresponds to the interatomic element linking α orbital at each atom. $\widehat{\chi}(N_{\rm d})$ is the reduced susceptibility. $g(\theta)$ is an angularly dependent embedding function for each type of the bond. The form for g as a function of bond angle θ and the procedure for the calculation of the coefficients is given in the reference by Pettifor [4] and the resulting embedding function curves for d are presented in the literature by Nishitani et al [7].

The TBB interactions for the fcc structure of Al are assumed to be negligible except for the first-nearest-neighbour, as the contributions from the further nearest-neighbours are expected to be small in the case of TBB interactions. The contributions from the second-, third- and fourth- nearest-neighbours are 3.28, 0.41 and 0.11% of the first-nearest-neighbour interaction respectively. They are easily absorbed by adjusting fitting parameters.

$N_{\rm s}$ and $N_{\rm d}$ are set as 2.62 and 0.38 respectively. These values are taken from the LMTO calculation of the electronic structure [8].

The hybridized NFE-TBB potential used in the present study is determined by three adjustable parameters, $r_{\rm c}$, D and $r_{\rm d}$. These parameters are set as the interatomic spacing d, the bulk modulus B and the trigonal shear constant C_{44} to be reproduced.

The elastic constants are derived as follows. The second derivative of the binding energy per atom U for a certain deformation of the lattice structure is assumed to be written as the sum of the second derivatives of the interatomic potential. Then, $C' = 1/2(C_{11} - C_{12})$ and C_{44}, which are given by the second derivative

of the binding energy with appropriate deformations, can be evaluated from the interatomic potentials. These constants are given by the following relations.

$$C_\lambda = \frac{1}{12\Omega}\frac{d^2U(\gamma_\lambda)}{d\gamma_\lambda^2} \quad (\lambda = 1, 2), \tag{4.6}$$

where $C_\lambda \quad (\lambda = 1, 2)$ correspond to C' and C_{44} and Ω is the atomic volume. The deformation γ_λ are taken as the strain matrix elements introduced in the literature [9]. The bulk modulus B is derived from

$$B = \frac{1}{12\pi d}\left(\frac{d^2U}{dr^2}\right)_{r=d}, \tag{4.7}$$

where d is the equilibrium interatomic spacing.

The energy term which depends only on the atomic volume is not treated in addition to the present formulation of the effective interatomic potential even in our calculations of the bulk modulus. The validity of this assumption is argued in section VIII of the reference [1].

4.3 Results

If we fix all variables r and θ in equation 4.5 to the interatomic separation and the bond angle of the non-strained crystallographic structure respectively, the potential function ϕ results in a pairwise interaction. This pairwise interaction potential is used for the parameters fitting, as the interatomic separations and the bulk moduli are the same for the non-pairwise and the pairwise potential, for they depend only on r originated from an atom. The pairwise potential is also used for the fitting to the experimental C_{44}, but the agreements of the calculated C_{44} with the experimental data was very poor as we see later on. The same parameters sets showed much better agreements with the experimental C_{44} with the non-pairwise potentials.

The results of the fitting of the parameters in the potential functions are compiled in table 4.1 and 4.2. We adjusted parameters for the interactions model which includes the interactions up to first-, second-, third- or fourth-nearest neighbours respectively. The parameters do not vary very much with the interactions model.

The resulting interatomic potential calculated using the parameters set for the fourth-nearest-neighbour interactions model is given in figure 4.1. The potential

Table 4.1 The results of the fitting of the adjustable parameters. The numbers given in the first column are the number of the outermost nearest neighbour shell included.

Nearest Neighbour	r_{c} Å	D	r_{d} Å
1	0.7629	0.3827	1.2086
2	0.7515	0.3631	1.2396
3	0.7682	0.4025	1.1864
4	0.7659	0.3871	1.2075

Table 4.2 Calculated and experimentally determined elastic constants C_{ij}, the result of the fitting and the experimental data for the interatomic separations d and the bulk moduli B for the fcc Al at 0K. The experimental data for d is calculated from the experimental lattice constant [10] and B is taken from the literature [11]. Calculated also are the elastic constants obtained by the pairwise potentials with fixed bond order. Model 'n' and 'p' stand for the non-pairwise and the pairwise potential respectively. The parameters used are those compiled in table 4.1 and the same for the present two models. Experimental data are taken from the literature [11]. The numbers given in the first column are the number of the outermost nearest neighbour shell included.

Nearest Neighbour	Model	C_{11} GPa	C_{12} GPa	C_{44} GPa	B GPa	C' GPa	$C_{12}-C_{44}$ GPa	d Å
1	n	102.62	69.34	42.20	80.43	16.64	27.15	2.8605
	p	120.12	60.59	59.18	80.43	29.77	1.41	2.8605
2	n	110.30	66.18	36.60	80.89	22.06	29.58	2.8595
	p	129.19	56.74	54.92	80.89	36.23	1.81	2.8595
3	n	111.43	65.02	39.22	80.49	23.20	25.80	2.8608
	p	127.99	56.74	55.29	80.49	35.62	1.45	2.8608
4	n	110.17	65.04	38.26	80.08	22.57	26.78	2.8614
	p	127.63	56.31	55.20	80.08	35.66	1.11	2.8614
Experimental		114.30	61.92	31.62	79.38	26.19	30.30	2.8634

curve shown in figure 4.1 is derived with the bond orders for the bonding with the first-nearest-neighbour atom and the same curve shows the angular-dependent non-pairwise potential describing first-nearest-neighbour bond direction and the angular-independent pairwise potential at the same time.

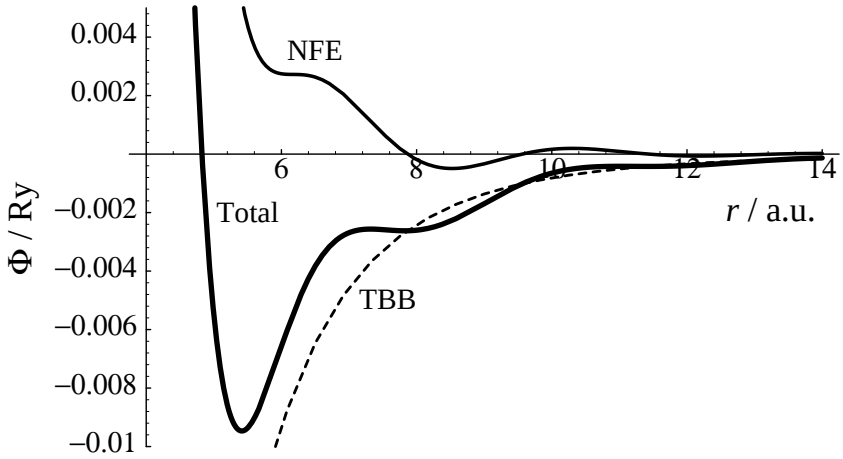

Figure 4.1 Interatomic potential for Al at 0K. Potential energy curve toward first-nearest-neighbour bond direction. The parameters set used is that for the fourth-nearest-neighbour interactions model.

The change of the binding energy versus tetragonal or trigonal strain calculated from the non-pairwise fourth-nearest-neighbour interactions model interatomic potential is given in figure 4.2. The second-order polynomial fit shown in the figure is obtained by a least-square fitting to the plotted binding energy change.

The elastic constants calculated using these parameters set is also given in table 4.2. The non-pairwise and the pairwise potentials show remarkable difference in agreements between the calculated and the experimental data for tetragonal shear constants C'. Combined with the good agreements accomplished in the fitting to the experimental trigonal constants C_{44}, we can say that the angular-dependence of the d-bonding interactions in the non-pairwise potential model have greatly improved the reproducibility of the experimental elastic constants data. On the other hand, the inclusion of the long-range interactions does not improve the reproducibility much. This fact that the angular-dependence of the

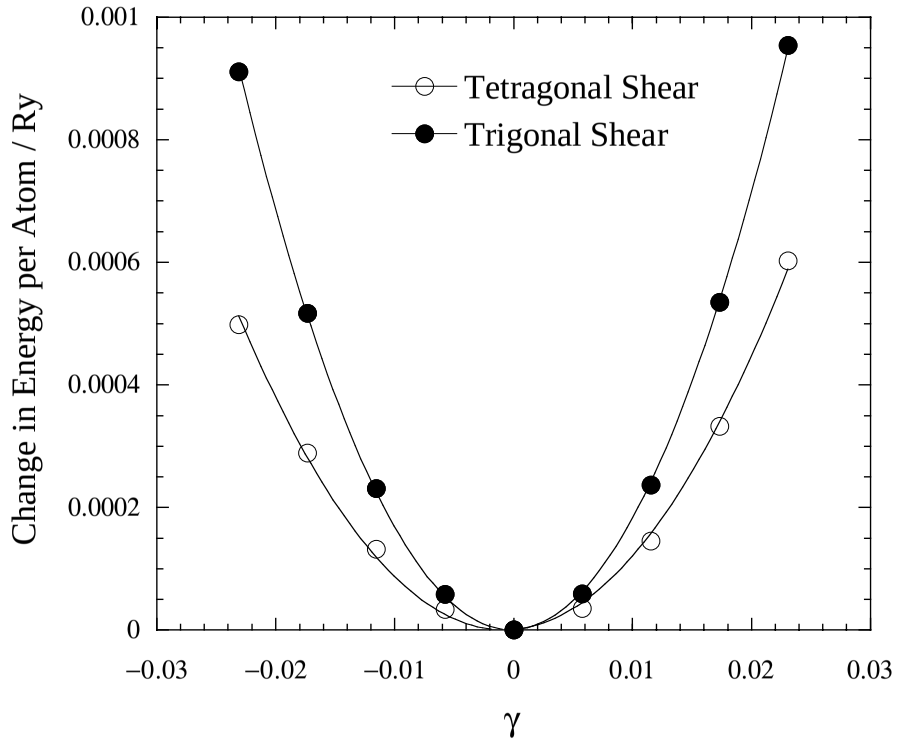

Figure 4.2 Change of the binding energy per atom as function of γ for tetragonally and trigonally deformed fcc Al. The curves given are second-order polynomial fits. The parameters set used is that for the fourth-nearest-neighbour interactions model.

bonding is more important in determining the elastic constants than the long-range interactions is also observed for the light-actinide metals [12].

The bcc-fcc and the hcp-fcc energy difference are also evaluated for each nearest-neighbour interactions model and the results are given in table 4.3. For bcc case, TBB interactions are included up to the second-nearest neighbours. The binding energies for the fcc and the hcp structures are exactly the same for the first- and the second-nearest-neighbour interactions model. The relative structural stability of the fcc structure of Al compared with bcc or hcp structures are recovered by including the long-range interactions just like the original NFE potential for Al by Pettifor and Ward [5]. In the present case, this is accomplished by the fourth-nearest-neighbour interactions for fcc structure.

Table 4.3 Energy differences for bcc and hcp structures compared with fcc structure. The numbers given in the first column are the number of the outermost nearest neighbour shell included.

Nearest Neighbour	$\Delta E_{\rm bcc}$ mRy/atom	$\Delta E_{\rm hcp}$ mRy/atom
1	14.07	0
2	10.63	0
3	3.22	-0.10
4	3.28	0.68

4.4 Conclusions

Presented in this chapter is a hybridized NFE-TBB interatomic potential model for Al. By including the short-range d-electrons angular-dependent bonding interactions, very good agreements of the calculated elastic constants with the experimental data are accomplished, which are not accomplished with the NFE pair-potential only. With the NFE pair-potential only, I have derived the calculated elastic constants data as follows by the same procedure: $C' = 27.12$GPa, $C_{44} = 32.86$GPa and $B = 44.00$GPa with $r_c = 0.6917$Å, D =0. These data clearly mean that I cannot fit to the experimental elastic constants data with the pair-potential only in this case.

Obtained also is a correct structural stability order in bcc, fcc and hcp structures for Al. This is accomplished by including the long-range interactions, at

least, up to the fourth-nearest-neighbours, as was shown by the NFE pair-potential calculations [5] or more detailed calculations [3, 13].

With these two results, one can derive both efficient and proper interatomic potential function that can be used in the intensive molecular dynamics simulations within the angular-dependent hybridized NFE-TBB interaction framework, for the present model have the non-pairwise (i.e. slow to calculate) but short-range TBB part that can determine C_{ij} correctly and the long-range but pairwise (i.e fast to calculate) NFE part that can determine relative structural stability order correctly.

References

[1] J. M. Wills and W. A. Harrison, *Phys. Rev.* B**28** 4363 (1983).

[2] Ch. Hausleitner and J. Hafner, *Phys. Rev.* B**45** 115 (1992).

[3] S. R. Nishitani, *J. Phase Equilibria* **18** 546 (1997).

[4] D. G. Pettifor, *Many-Atom Interactions in Solids*, edited by R. M. Nieminen, M. J. Puska and M. J. Manninen (Springer-Verlag, Berlin, 1990) p 64.

[5] D. G. Pettifor and M. A. Ward, *Solid State Comm.* **49** 291 (1984).

[6] N. Singh, N. S. Banger and S. P. Singh, *Phys. Rev.* B**39** 3097 (1989).

[7] S. R. Nishitani, P. Alinaghian, C. Hausleitner and D. G. Pettifor, *Phil. Mag. Lett.* **69** 177 (1994).

[8] J. Hafner and S. S. Jaswal, *Phys. Rev.* B**38** 7320 (1988).

[9] P. Alinaghian, S. R. Nishitani and D. G. Pettifor, *Phil. Mag.* B**69** 889 (1994).

[10] P. Villars and L. D. Calvert, *Pearson's Handbook of Crystallographic Data for Intermetallic Phases, 2nd ed.* (ASM International, Materials Park, 1991).

[11] G. N. Kamm and G. A. Alers, *J. Appl. Phys.* **35** 327 (1964).

[12] K. Hachiya and Y. Ito, *Physica* B, in printing.

[13] A. K. McMahan and J. A. Moriarty, *Phys. Rev.* B**27** 3235 (1983).

Chapter 5

Hybridized NFE-TBB model of the bonding in the rare-earth metals

5.1 Introduction

For a few decades, bondings in simple metals have been successfully treated theoretically [1]. Harrison [2] applied one of the most simplified theory (Thomas-Fermi theory) for the simple metals and extended for the bondings in lanthanides and heavy actinides and made success in predicting the trends in some properties of these metals. His model treats the spd-electrons for all the f-shell metals as the sp-electrons for the simple metals and all f-bands are localized except for light-actinides. In this treatment, the interatomic interaction can be written as the single-term pairwise screened Coulomb potential same as the one for the simple metals by himself [3].

Based on the success of this model, Singh [4] applied the hybridized nearly-free-electron–tight-binding-bond (NFE-TBB) model of the two-body interaction on some of the fcc rare-earth metals originally developed by Wills and Harrison [5, 2] and attempted to make more realistic description of the bondings by treating the effect of the d-bands and f-bands explicitly. Using this model, they calculated the elastic constants and compared with the experimental data and showed reasonable accord.

Nevertheless, f-bands for the lanthanides and heavy-actinides can be seen as localized to a large extent [6] and it is questionable to treat the effect of the f-bands explicitly at this level of the approximation. Besides, although the model by Singh [4] has acquired some accuracy, no optimization of the tight-binding param-

eters are done and the accord with the experimental data are seems to be achieved through including many-nearest-neighbours interactions. Requiring many-nearest-neighbours bears problems as follows at least: (1) not always physical to include further neighbour interactions instead of the angular dependence of the bondings [8], and (2) hard to be used as interatomic potential functions in molecular dynamics simulations.

Motivated by these facts, the aim of this chapter is set to apply a simplified but realistic enough and physically appropriate interatomic potentials function for rare-earth metals and their compounds. The same formula using combined fourth-nearest-neighbour NFE and first-nearest-neighbour bond-angle-dependent TBB model is used as have already been tested for aluminium in chapter 4. By using such potential functions, we can model such as long time-scale dynamical properties or large-scale atomistic motions which is important for the understanding of the mechanical properties through molecular dynamics simulation.

The model and procedure used for the estimations of the elastic constants to be compared with the experimental data are described in the next section. Results of the derived elastic constants and the comparison with the available experimental data are presented in section 5.3. Conclusions are shown in section 5.4.

5.2 Computational method

The hybridized NFE-TBB model of the interatomic potential is as follows [9]:

$$\Phi_{\mathrm{total}} = \Phi_{\mathrm{NFE}} + \Phi_{\mathrm{TB,rep}} + \Phi_{\mathrm{TB,bond}}. \tag{5.1}$$

The first term treats the sp-electron gas in simple metal. The remaining terms are for the TBB part of the potential for the d-electrons in the present study, for I have assumed f-bands to be fully localized. This is a good approximation except for the low temperature phase of Ce. Thus, the interatomic potential mode used for the rare-earth metals is the same as the one for the transition metals.

The following NFE interaction formulation by Pettifor and Ward [10] is adopted;

$$\Phi_{\mathrm{NFE}} = \frac{2N_{\mathrm{s}}^2}{r_{ij}} \sum_{n=1}^{3} A_n \cos(k_n r + \alpha_n) \exp(\kappa_n r_{ij}). \tag{5.2}$$

N_{s} is the number of sp-valence electrons. Heine-Abarenkov model potential is used to calculate the parameters A_n, α_n, k_n and κ_n [11] and all of them are determined by r_{c} and D.

The following is the repulsive interaction used;

$$\Phi_{\mathrm{TB,rep}} = \frac{N_{\mathrm{d}}}{7}\frac{h_{ij}^2 d_{ij}^{10}}{r_{ij}^8}. \tag{5.3}$$

N_{d} is the number of d-valence electrons and is determined as the number of total valence electrons minus N_{s}. d_{ij} is the equilibrium interatomic separation. The interatomic matrix elements form obtained by Wills and Harrison [5] is used. All matrix elements and their average h are determined by a single parameter, r_{d}.

Bond energy expression is;

$$\Phi_{\mathrm{TB,bond}} = 2\sum_{\alpha\beta} H_{j\beta,i\alpha}\Theta_{i\alpha,j\beta}. \tag{5.4}$$

$H_{j\beta,i\alpha}$ is the tight-binding Hamiltonian and $\Theta_{i\alpha,j\beta}$ is the bond order. Bond order is calculated from the following simplified expression [13];

$$\Theta_{i,j}^{\alpha} = \widehat{\chi}(N_{\mathrm{d}}) \Bigg/ \left\{1 + \frac{1}{2}\sum_{k\neq i,j}\left[\left(\frac{h_\alpha(r_{ik})}{h_\alpha(r_{ij})}\right)^2 g_\alpha(\theta_{jik}) + \left(\frac{h_\alpha(r_{jk})}{h_\alpha(r_{ij})}\right)^2 g_\alpha(\theta_{ijk})\right]\right\}^{1/2}. \tag{5.5}$$

The suffix α denotes σ, π and δ orbitals, and h_α corresponds to the interatomic element linking α orbital at each atom. $\widehat{\chi}(N_{\mathrm{d}})$ is the reduced susceptibility. $g(\theta)$ is an angularly dependent embedding function for each type of the bond. The form for g as a function of bond angle θ and the procedure for the calculation of the coefficients are given in the reference by Pettifor [12] and the resulting embedding function curves for d are presented in the literature by Nishitani et al [13].

The TBB interactions are assumed to be negligible except for the first-nearest-neighbour as is done for the fcc structure of Al in chapter 4.

The NFE-TBB potential used in the present study is determined by three adjustable parameters, r_{c}, D and r_{d} if we fix N_{s} or N_{d}. These parameters are set as the interatomic spacing d and the bulk modulus B to be reproduced by the least-square fitting. Several starting values are taken for these parameters set for each atom around the final values reported in the literature [4] and chose one which gained the best accord with experimental elastic constants data. Total numbers of valence electrons are 3 for all metals except the one for Yb which is 2. Numbers for N_{d} is 1 except for those for γ-Ce and β-Yb, which are 0.5 and 0.1 respectively. The value $N_{\mathrm{d}} = 1$ for these two metals gives a very poor results for C'.

If we fix all variables r and θ in equation 5.5 to the interatomic separations and the bond angles of the non-strained crystallographic structure respectively, the potential function ϕ results in a pairwise interaction. This pairwise interaction potential is used for the parameters fitting, as the interatomic separations and the bulk moduli are assumed to be the same for the non-pairwise and the pairwise potential. This is true for the cubic crystals and approximately true for the hexagonal crystals. The error arises from this assumption for the hexagonal crystals is less than 1% for all hexagonal metals, which is evaluated using homogenous strain matrix [7] and the equation corresponding to equation 5.6 which will be introduced later on.

The elastic constants are derived as follows. The second derivative of the binding energy per atom U for a certain deformation of the lattice structure is assumed to be written as the sum of the second derivatives of the interatomic potential. Then, for cubic crystals, $C' = 1/2(C_{11} - C_{12})$ and C_{44}, which are given by the second derivative of the binding energy with appropriate deformations, can be evaluated from the interatomic potentials. These constants are given by the following relations.

$$C_\lambda = \frac{1}{12\Omega}\frac{d^2U(\gamma_\lambda)}{d\gamma_\lambda^2} \quad (\lambda = 1, 2), \tag{5.6}$$

where $C_\lambda \quad (\lambda = 1, 2)$ correspond to C' and C_{44}, and Ω is the atomic volume. The deformation γ_λ are taken as the strain matrix elements introduced in the literature [8]. The bulk moduli B are derived from

$$B = \frac{1}{12\pi d}\left(\frac{d^2U}{dr^2}\right)_{r=d}, \tag{5.7}$$

where d is the equilibrium interatomic spacing.

For hexagonal crystals, elastic constants can be evaluated using the strain matrices introduced by Cohen, Stixrude and Wasserman [14], for example. Their matrices for C_{66}, C_{44} and C_S are used in this calculations, but C_{33} is determined instead of R using the following strain matrix

$$\epsilon = \begin{pmatrix} 0 & 0 & 0 \\ 0 & 0 & 0 \\ 0 & 0 & \gamma \end{pmatrix}, \tag{5.8}$$

which gives C_{33} as

$$C_{33} = \frac{1}{\Omega}\frac{d^2U(\gamma)}{d\gamma^2}. \tag{5.9}$$

The bulk moduli B for hexagonal crystals are derived in the same way as for cubic crystals. C_{11}, C_{12} and C_{13} are calculated from the following relations:

$$C_{11} = \frac{1}{2}C_{\mathrm{S}} + C_{33} - \sqrt{2C_{\mathrm{S}}(C_{33} - B)} + C_{66}, \tag{5.10}$$

$$C_{12} = \frac{1}{2}C_{\mathrm{S}} + C_{33} - \sqrt{2C_{\mathrm{S}}(C_{33} - B)} - C_{66}, \tag{5.11}$$

$$C_{13} = C_{33} - \sqrt{\frac{1}{2}C_{\mathrm{S}}(C_{33} - B)}. \tag{5.12}$$

5.3 Results

Room temperature phases of the rare earth metals (Sc, Y, Ce, Pr, Nd, Gd, Tb, Dy, Ho, Er, Yb, Lu) and high temperature cubic phase of La (fcc La, β-phase) are chosen for fitting parameters for the interatomic potentials because of the availability of the experimental elastic constants data as far as I know.

The final values for the parameters set for each metal is compiled in table 5.1 and the interatomic potentials calculated using the final parameters set for β-La are present in figure 5.1. The potential curve shown in figure 5.1 is derived with the bond orders for the bonding with the first-nearest-neighbour atoms. Consequently, the same curve shows the angular-dependent non-pairwise potential describing first-nearest-neighbour bond axis direction and the angular-independent pairwise potential for all directions at the same time.

The change of the binding energy versus tetragonal or trigonal shear strain calculated with the non-pairwise interactions potential model for β-La is given in figure 5.2. The second-order polynomial fit shown in the figure is obtained by a least-square fitting to the plotted binding energy change.

The elastic constants calculated using these binding energy curves are given in table 5.2 and 5.3 with the experimental data. The calculated and experimental elastic constants data show good agreements for all the rare-earth metals as a whole as shown in figure 5.3, but the data for C_{44} do not show good accord as the other constants. Our choice of the model and the parameters almost always result in the too much lower calculated values. The non-pairwise and the pairwise potentials show some difference in agreements between the calculated and the experimental data for tetragonal shear constants C' for cubic metals or C_{66} for hexagonal metals. The difference is also shown in C_{44}. The non-pairwise potentials give lower values of C_{44} compared with those with the pairwise potentials. This means that the effect of the non-pairwise interactions do exist, but it is more

Table 5.1 Number of valence electron used in the present calculations and the final values of the interatomic potential parameters for the rare-earth metals derived by fitting to the experimental data of the elastic constants. Also shown are the crystal structure for each phase. The names of the element without any phase specifications are room-temperature phases.

	N	N_{s}	N_{d}	r_{c} [Å]	D	r_{d} [Å]	Structure
Sc	3	2	1	0.9009	0.1989	0.9898	hcp
Y	3	2	1	0.9145	0.0289	0.5132	hcp
β-La	3	2	1	1.1679	0.5826	0.8830	fcc
γ-Ce	3	2.5	0.5	1.1689	0.7861	0.8389	fcc
Pr	3	2	1	1.0210	0.3776	0.6283	dhcp
Nd	3	2	1	1.0225	0.3540	0.7406	dhcp
Gd	3	2	1	0.9666	0.1688	0.7955	hcp
Tb	3	2	1	0.9397	0.1656	0.6906	hcp
Dy	3	2	1	0.9266	0.1209	0.7005	hcp
Ho	3	2	1	0.9016	0.0843	0.5869	hcp
Er	3	2	1	0.9029	0.0536	0.7186	hcp
β-Yb	2	1.9	0.1	1.2036	0.6764	0.7291	fcc
Lu	3	2	1	0.9170	0.1989	0.8397	hcp

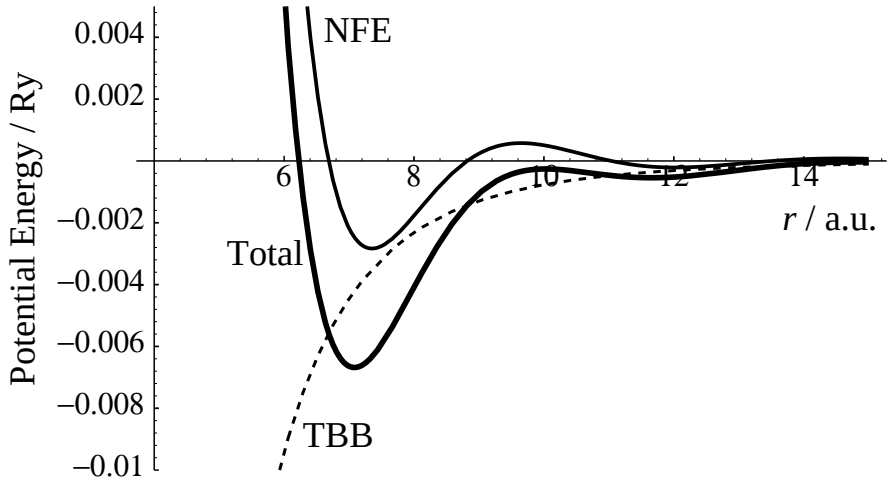

Figure 5.1 Interatomic potential for β-La calculated with the final set of parameters.

complicated than I have assumed. There may be higher moments to be included in the evaluation of the bond orders of the bondings in these metals.

Although the effect of the angular-dependence of the d-bond is revealed, it is not so evident as the transition metals or the light-actinide metals, for example. The relatively weak dependence on the angular-dependent d-bond in the rare-earth metals corresponds to the small values of $r_{\rm d}$ in table 5.1 compared with those of the transition metals [9]. This means that the d-bands in the rare-earth metals are narrow compared with those in the transition metals. Therefore, the d-bondings in the rare-earth metals play a non-negligible but relatively small role.

For the practical use as a potential function in molecular dynamics simulations, the pairwise model may be used instead of the non-pairwise model as the calculated data show the better accord with experimental data compared with the case of the transition metals. In addition, one may be able to adopt shorter cutoff radii of the potentials. As shown for Al in chapter 4, we can easily fit to the equilibrium interatomic separations and the elastic constants (i.e. the second derivative of the potential) are insensitive to the number of the nearest-neighbours included. Therefore, we can expect that the force acts, at least, near the equilibrium atomic positions can be calculated exactly enough.

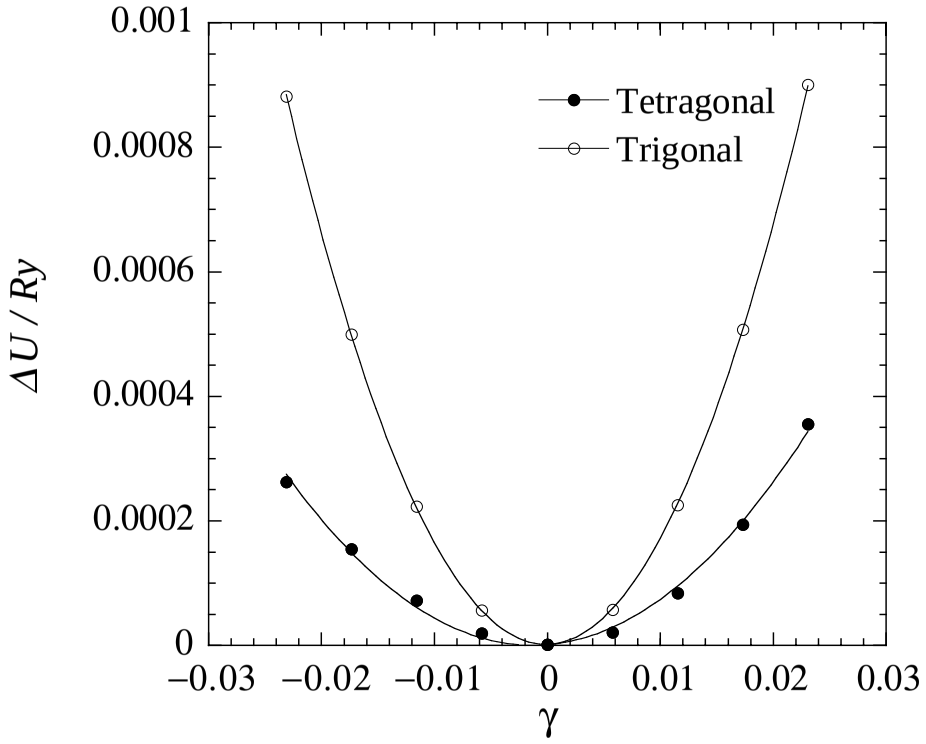

Figure 5.2 Change of the binding energy per atom as function of γ for tetragonally and trigonally deformed β-La. The curves given are second-order polynomial fits.

Table 5.2 Calculated and experimentally determined elastic constants C_{ij} [GPa], the result of the fitting and the experimental data for the interatomic separations d [a.u.] and the bulk moduli B [GPa] for the cubic crystals. The experimental data for d are calculated from the experimental lattice constant [15]. Calculated also are the elastic constants obtained by the pairwise potentials with fixed bond order. Model 'n' and 'p' stand for the non-pairwise and the pairwise potential respectively. The parameters used are those compiled in table 5.1 and the same for the present two models.

		C_{11}	C_{12}	C_{44}	B	C'	d
β-La	n	30.66	19.32	16.37	23.10	5.67	7.0705
	p	32.57	18.37	18.22	23.10	7.10	7.0705
	Expt.[a]	28.46	20.41	16.53	23.09	4.03	7.0707
γ-Ce	n	26.87	13.67	12.08	18.07	6.60	6.8913
	p	27.96	13.13	13.14	18.07	7.42	6.8913
	Expt.[b]	26.01	14.26	17.30	18.18	5.88	6.8891
β-Yb	n	18.59	10.26	10.04	13.04	4.17	7.3297
	p	18.73	10.19	10.18	13.04	4.27	7.3297
	Expt.[c]	18.62	10.36	17.72	13.11	4.13	7.3270

a : Elastic constants data from [16] (660K), b : Elastic constants data from [17], c : Elastic constants data from [18].

Table 5.3 Calculated and experimentally determined elastic constants C_{ij} [GPa], the result of the fitting and the experimental data for the interatomic separations d [a.u.] and the bulk moduli B [GPa] for the hexagonal crystals. The experimental data for d and c/a are calculated from the experimental lattice constant [15]. Calculated also are the elastic constants obtained by the pairwise potentials with fixed bond order. Model 'n' and 'p' stand for the non-pairwise and the pairwise potential respectively. The parameters used are those compiled in table 5.1 and the same for the present two models.

		C_{11}	C_{12}	C_{13}	C_{33}	C_{44}	B	C_{66}	d	c/a
Sc	n	103.0	40.4	31.0	100.9	21.9	56.72	31.3	6.251	1.584
	p	109.4	33.8	27.0	116.1	30.1	56.72	37.8	6.251	1.584
	Expt.[a]	98.6	44.8	29.5	106.2	27.5	56.72	26.9	6.251	1.592
Y	n	76.60	27.41	21.09	80.59	19.71	41.43	24.59	6.90036	1.61334
	p	77.06	27.01	20.83	81.47	20.18	41.43	25.02	6.90036	1.61334
	Expt.[b]	77.90	28.50	21.00	76.90	24.31	41.43	24.70	6.90038	1.57399
Pr	n	54.19	21.18	14.58	51.55	11.06	28.80	16.50	6.9400	1.6275
	p	55.10	20.59	14.09	52.72	11.46	28.80	17.26	6.9400	1.6275
	Expt.[c]	49.35	22.95	14.3	57.40	13.60	28.80	13.20	6.9400	1.6114
Nd	n	59.47	23.63	16.40	56.02	12.17	31.78	17.92	6.9131	1.6264
	p	60.88	22.52	15.41	58.83	12.94	31.78	19.18	6.9131	1.6264
	Expt.[d]	54.82	24.62	16.6	60.86	15.03	31.79	15.10	6.9130	1.6124
Gd	n	69.73	25.44	19.41	72.62	17.11	37.83	22.15	6.8654	1.6179
	p	70.86	24.48	18.78	74.73	18.26	37.83	23.19	6.8654	1.6179
	Expt.[b]	66.67	24.99	21.32	71.91	20.69	37.83	20.84	6.8654	1.5893
Tb	n	71.25	26.55	19.97	73.28	17.34	38.72	22.35	6.80496	1.61906
	p	72.51	25.47	19.26	75.62	18.63	38.72	23.52	6.80496	1.61906
	Expt.[e]	67.88	24.32	22.99	72.25	21.40	38.78	21.78	6.80496	1.58111
Dy	n	75.94	25.39	21.01	83.08	28.09	41.07	25.28	6.7896	1.5842
	p	69.63	16.64	29.08	110.97	29.49	41.07	26.49	6.7896	1.5842
	Expt.[b]	74.66	26.16	22.33	78.71	24.27	41.07	24.25	6.7896	1.5732
Ho	n	71.16	23.48	24.41	82.08	20.15	40.81	23.84	6.7601	1.5808
	p	71.93	22.76	24.02	83.89	21.09	40.81	24.58	6.7601	1.5808
	Expt.[f]	76.12	26.00	20.72	80.15	25.92	40.81	25.06	6.7601	1.5698
Er	n	82.70	30.22	24.38	85.99	21.73	45.47	26.24	6.7252	1.5810
	p	82.35	27.02	25.38	89.31	23.51	45.47	27.66	6.7252	1.5810
	Expt.[b]	86.34	30.50	22.70	85.54	28.09	45.47	27.92	6.7252	1.5700
Lu	n	87.00	33.05	24.94	88.87	26.97	47.59	26.97	6.6326	1.5860
	p	86.72	27.77	25.24	100.36	30.11	47.59	29.48	6.6326	1.5860
	Expt.[g]	86.23	32.03	28.0	80.86	26.79	47.59	27.10	6.6326	1.5860

a : Elastic constants data from [19] (303K), b : Elastic constants data from [20] (298.0K),
c : Elastic constants data from [21] (300K), d : Elastic constants data from [22] (300K),
e : Elastic constants data from [23] (300K), f : Elastic constants data from [24] (300K),
g : Elastic constants data from [25] (300.1K).

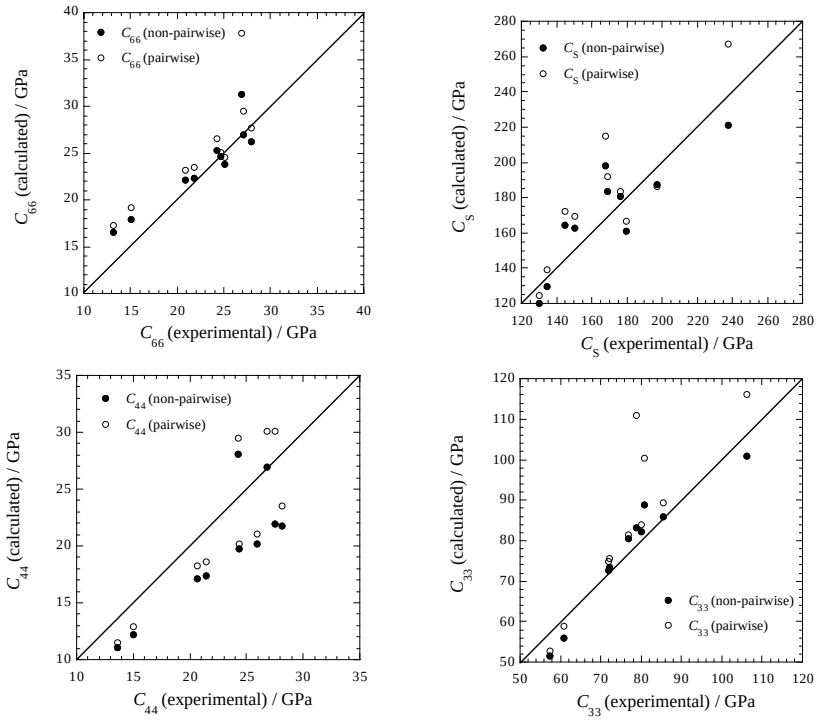

Figure 5.3 Plots of the experimental versus calculated elastic constants for C_{66} (upper left panel), C_{44} (lower left panel), C_{S} (upper right panel) and C_{33} (lower right panel).

5.4 Conclusions

Presented in this chapter are the hybridized NFE-TBB potentials for the rare-earth metals and their compounds and tested through the comparison between calculated and experimental elastic constants data.

We can successfully fit to or reproduce the experimental data for the equilibrium interatomic separations, bulk moduli and elastic constants for the cubic and the hexagonal crystals, and c/a ratio for the hexagonal crystals with the present potentials model.

The bondings in the rare-earth metals are proved to depend on the angular-dependence of the d-bond, but they are obscure compared with those in the transition metals.

The interatomic interactions model used in the present study based on the angular-dependent second-moment approximation of the bond order, but the higher orders of moment may be needed especially for the prediction of the C_{44} of the cubic crystals which have highly negative Cauchy pressure ($C_{12} - C_{44}$), such as γ-Ce or β-Yb.

The model presented and tested in the present study must be easily extended to the rare-earth compounds as has been demonstrated for the transition metals [9, 26].

References

[1] W. A. Harrison, *Electronic Structure and the Properties of Solids* (Freeman, New York, 1980).

[2] W. A. Harrison, *Phys. Rev.* B**28** 550 (1983).

[3] W. A. Harrison and J. M. Wills, *Phys. Rev.* B**25** 5007 (1982).

[4] N. Singh and S. P. Singh, *Phys. Rev.* B**42** 1652 (1990).

[5] J. M. Wills and W. A. Harrison, *Phys. Rev.* B**28** 4363 (1983).

[6] W. A. Harrison, *Phys. Rev.* B**29** 2917 (1984).

[7] H. Hasegawa, M. W. Finnis and D. G. Pettifor, *J. Phys. F: Met. Phys.* **15** 19 (1985).

[8] P. Alinaghian, S. R. Nishitani and D. G. Pettifor, *Phil. Mag.* B**69** 889 (1994).

[9] Ch. Hausleitner and J. Hafner, *Phys. Rev.* B**45** 115 (1992).

[10] D. G. Pettifor and M. A. Ward, *Solid State Commun.* **49** 291 (1984).

[11] N. Singh, N. S. Banger and S. P. Singh, *Phys. Rev.* B**39** 3097 (1989).

[12] D. G. Pettifor, *Many-Atom Interactions in Solids*, edited by R. M. Nieminen, M. J. Puska and M. J. Manninen (Springer-Verlag, Berlin, 1990) p 64.

[13] S. R. Nishitani, P. Alinaghian, C. Hausleitner and D. G. Pettifor, *Phil. Mag. Lett.* **69** 177 (1994).

[14] R. E. Cohen, L. Stixrude and E. Wasserman, *Phys. Rev.* B**56** 8575 (1997).

[15] P. Villars and L. D. Calvert, *Pearson's Handbook of Crystallographic Data for Intermetallic Phases, 2nd ed.* (ASM International, Materials Park, 1991).

[16] C. Stassis, C.-K. Loong and J. Zarestky, *Phys. Rev.* B**26** 5426 (1982).

[17] J. D. Greiner, O. D. McMasters and J. F. Smith, *Scr. Metall.* **14** 989 (1980).

[18] C. Stassis, C.-K. Loong, C. Theisen and R. M. Nicklow, *Phys. Rev.* B**26** 4106 (1982).

[19] R. G. Leisure, R. B. Schwarz, A. Migliori and M. Lei, *Phys. Rev.* B**48** 1276 (1993).

[20] G. Simmons and H. Wang, *Single Crystal Elastic Constants and Calculated Aggregate Properties: A Handbook* (MIT Press, Cambridge, 1971).

[21] J. D. Greiner, R. J. Schiltz, Jr., J. J. Tonnies, F. H. Spedding and J. F. Smith, *J. Appl. Phys.* **44** 3862 (1973).

[22] J. D. Greiner, D. M. Schlader, O. D. McMasters, K. A. Gschneidner, Jr. and J. F. Smith, *J. Appl. Phys.* **47** 3427 (1976).

[23] K. Salama, F. R. Brotzen and P. L. Donoho, *J. Appl. Phys.* **43** 3254 (1972).

[24] K. Salama, F. R. Brotzen and P. L. Donoho, *J. Appl. Phys.* **44** 180 (1973).

[25] J. J. Tonnies, K. A. Gschneidner, Jr. and F. H. Spedding, *J. Appl. Phys.* **42** 3275 (1971).

[26] K. Hachiya and Y. Ito, *J. Alloys Compounds* **279** 171 (1998).

Chapter 6

Hybridized NFE-TBB model of the bonding in C15 Laves phase structure Al–rare-earth intermetallic compounds

6.1 Introduction

Among the structures of the intermetallic phase, many compounds have the structures which are known as Laves phase. This is one of the most common structures of the binary intermetallic compounds. Half of them have the cubic phase structure, which is called as Cu_2Mg-type or C15 structure.

The elastic constants are both fundamentally and practically useful physical properties not only as themselves but as those closely related to lattice dynamics, phase stability, etc., as they determine the curvature of the binding energy toward a certain direction. Although the experimental data available for the elastic constants of the intermetallic compounds at present are limited compared with their enormous number of the combination of the elements which can form binary intermetallic compounds, the data are continuously accumulated. As for C15 Laves phase compounds, some data are available including the series of data for Al_2M ($M =$ rare earth elements) [1].

In the present chapter, this type of the intermetallic compounds is chosen as a test of the interatomic potentials functions for the binary intermetallic compounds which are determined from those of the component elements metals because of

the availability of the experimental data to be compared with the calculated elastic constants.

The interatomic potentials model used in this chapter is the hybridized nearly-free-electron–tight-binding-bond (NFE-TBB) model potential developed by Hausleitner and Hafner [2]. Here, a procedure for constructing a hybridized NFE-TBB model potential for Al-M (M = Nd, Pr) intermetallic compounds is presented using tight-binding (TB) parameters already derived for the same potential model for pure Al and rare-earth metals in chapter 4 and 5. The major difference between the model used in this chapter and the original model by Hausleitner and Hafner is the inclusion of the explicit angular-dependence of the bonding in the bond order. The bond order in the original model has an expression with the Bethe lattice, as it is designed for the disordered alloy. The simplified formula for the bond order derived by Pettifor and co-workers [3, 4] is used and shown that the bondings in the metals depend more on the angular-dependence of the bonding than on the range of the interatomic interactions.

The purpose of the present chapter is to show the validity of the model used for the pure metals to the intermetallic compounds and the transferability of the TB parameters derived for the pure metals. As we will see later on, once parameters for metals A and B are known, we can construct a potential for the A-B compounds if the data of the structures and the d-state energies for A, B and A-B compounds are available.

The potential model used and the procedure for deriving parameters for binary compounds are given in the next section. Results are shown in section 6.2. Conclusions are presented in section 6.4.

6.2 Computational method

The hybridized NFE-TBB model of the interatomic potential is as follows [2]:

$$\Phi_{\mathrm{total}} = \Phi_{\mathrm{NFE}} + \Phi_{\mathrm{TB,rep}} + \Phi_{\mathrm{TB,bond}}. \tag{6.1}$$

The first term treats the sp-electron gas in simple metal. The remaining terms are for the TBB part of the potential for the d-electrons in the present study. As the f-bands in all rare-earth atoms are assumed to be fully localized and the effect of the d-band in aluminium is assumed to be non-negligible, we can treat all interatomic interactions in Al-M as those in transition-metal intermetallic compounds.

The following NFE interaction formulation by Pettifor and Ward [5] is adopted;

$$\Phi_{\rm NFE} = \frac{2N_{{\rm s},i}N_{{\rm s},j}}{r_{ij}} \sum_{n=1}^{3} A_n \cos(k_n r + \alpha_n) \exp(\kappa_n r_{ij}). \tag{6.2}$$

$N_{\rm s}$ is the number of sp-valence electrons. Heine-Abarenkov model potential is used to calculate the parameters A_n, α_n, k_n and κ_n [6] and all of them are determined by $r_{\rm c}$ and D.

The following is the repulsive interaction used;

$$\Phi_{\rm TB,rep} = \frac{\sqrt{N_{{\rm d},i}N_{{\rm d},j}}}{7} \frac{h_{ij}^2 d_{ij}^{10}}{r_{ij}^8}. \tag{6.3}$$

$N_{\rm d}$ is the number of d-valence electrons and is determined as the number of total valence electrons minus $N_{\rm s}$. d_{ij} is the equilibrium interatomic separation. The interatomic matrix elements form obtained by Wills and Harrison [7] is used. All matrix elements and their average h are determined by a single parameter, $r_{\rm d}$.

Bond energy expression is;

$$\Phi_{\rm TB,bond} = 2 \sum_{\alpha\beta} H_{j\beta,i\alpha} \Theta_{i\alpha,j\beta}. \tag{6.4}$$

$H_{j\beta,i\alpha}$ is the tight-binding Hamiltonian and $\Theta_{i\alpha,j\beta}$ is the bond order. Bond order is calculated from the following simplified expression [4];

$$\Theta_{i,j}^{\alpha} = \widehat{\chi}(\sqrt{N_{{\rm d},i}N_{{\rm d},j}}) \Bigg/ \left\{ 1 + \frac{1}{2} \sum_{k\neq i,j} \left[\left(\frac{h_\alpha(r_{ik})}{h_\alpha(r_{ij})} \right)^2 g_\alpha(\theta_{jik}) + \left(\frac{h_\alpha(r_{jk})}{h_\alpha(r_{ij})} \right)^2 g_\alpha(\theta_{ijk}) \right] \right\}^{1/2}. \tag{6.5}$$

The suffix α denotes σ, π and δ orbitals, and h_α corresponds to the interatomic element linking α orbital at each atom. $\widehat{\chi}$ is the reduced susceptibility. $g(\theta)$ is an angularly dependent embedding function for each type of the bond [4].

The TBB interactions are assumed to be negligible except for the first-nearest-neighbour as is done for the pure metals in chapter 4 and 5.

The hybridized NFE-TBB potential used in the present study is determined by three adjustable parameters, $r_{\rm c}$, D and $r_{\rm d}$ if we fix $N_{\rm s}$ or $N_{\rm d}$. These parameters are determined by fitting calculated interatomic separations d and bulk modulus B to the experimental data. For Al-Al and M-M interactions, the values derived for pure Al and M metals respectively for $r_{\rm d}$ and D are used. The remaining parameter, $r_{\rm c}$ was determined by fitting to the experimental $d_{\rm Al-Al}$ or d_{M-M}. The

parameters for Al-M interaction was determined by fitting to experimental $d_{\mathrm{Al}-M}$ and B. First, r_{d} is derived for Al-M as a geometric mean of those for Al-Al and M-M. Then, r_{c} and D are determined by fitting to $d_{\mathrm{Al}-M}$ using $\Phi_{\mathrm{Al}-M}$ and by fitting to B using second derivative of the total binding energy calculated from determined Al-Al, M-M interactions potentials and undetermined Al-M interactions potential.

The numbers of valence electrons, N_{s} and N_{d}, for binary intermetallic compounds can be readily determined from the numbers of valence electrons for the pure metals [10] using a procedure described by Hausleitner and Hafner [2] and a simplified approximation for the d-band shape such as the rectangular band model [8], if the data for the d-state energies are available. (See Appendix A.) Here, N_{s} and N_{d} are determined by changing N_{s} for Al by 0.05 step under the following constraints.

$$\Delta N_{\mathrm{s},\alpha} + \Delta N_{\mathrm{d},\alpha} = 0, \qquad \alpha = \text{Al}, M, \tag{6.6}$$

$$x_{\mathrm{Al}}\Delta N_{\mathrm{d,Al}} + x_M \Delta N_{\mathrm{d},M} = 0, \tag{6.7}$$

where x_{Al} and x_M are the concentrations of Al and M.

If we fix all variables r and θ in equation 6.5 to the interatomic separations and the bond angles of the non-strained crystallographic structure respectively, the potential function Φ results in a pairwise interaction. This pairwise interaction potential is used for the parameters fitting, as the interatomic separations and the bulk moduli are exactly the same for the non-pairwise and the pairwise potential with the same parameters set.

The elastic constants are derived as follows. The second derivative of the binding energy per unit cell U for a certain deformation of the lattice structure is assumed to be written as the sum of the second derivatives of the interatomic potential. Then, for cubic crystals, $C' = 1/2(C_{11} - C_{12})$ and C_{44}, which are given by the second derivative of the binding energy with appropriate deformations, can be evaluated from the interatomic potentials. These constants are given by the following relations.

$$C_\lambda = \frac{1}{12V}\frac{d^2U(\gamma_\lambda)}{d\gamma_\lambda^2} \quad (\lambda = 1, 2), \tag{6.8}$$

where $C_\lambda \quad (\lambda = 1, 2)$ correspond to C' and C_{44}, and V is the volume of the unit cell. The deformation γ_λ are taken as the strain matrix elements introduced in the literature [9]. The bulk moduli B are derived from

$$B = \frac{1}{12\pi d}\left(\frac{d^2U}{dr^2}\right)_{r=d}, \tag{6.9}$$

where d is the equilibrium interatomic separations.

6.3 Results

6.3.1 Interatomic Potentials for Al_2Nd

As have been mentioned in the preceding sections, we can determine the numbers of valence electrons for the Al-M intermetallic compounds from those for the pure metals, if we fix N_{s} for Al, for example. Once N_{s} and N_{d} are derived, we can adjust all potential parameters by fitting. Here, $N_{\mathrm{s,Al}}$ is set as 2.72 and derived $N_{\mathrm{d,Al}} = 0.28$, $N_{\mathrm{s,Nd}} = 1.80$ and $N_{\mathrm{d,Nd}} = 1.20$ by the equations 6.6 and 6.7.

The adjusted parameters are compiled in table 6.1 and results of the fittings to the interatomic separations and the bulk modulus are compiled in table 6.2. The experimental data used are those at room temperature. The interatomic potentials derived with these final set of parameters are shown in figure 6.1.

Table 6.1 Adjusted interatomic potential parameters for Al_2Nd phase at 300K.

	Al-Al	Al-Nd	Nd-Nd
r_{c} [Å]	0.75891	0.86133	0.91427
D	0.40489	0.15030	0.35395
r_{d} [Å]	1.19346	0.94018	0.74065

The calculated elastic constants data are compiled in table 6.2. These data are obtained from the second derivatives of the second-order polynomial fits at $\gamma = 0$. The changes of the binding energy against deformations are shown in figure 6.2. The equilibrium position toward the trigonal shear deformation is shifted approximately ± 0.2% in each cases. The reproducibility of the C' was very good especially for the non-pairwise interactions potential. Along with the perfect fitting to the bulk modulus, a very good agreement of the calculated and the experimental C_{11} and C_{12} is achieved. Compared with the results obtained by the pairwise potential with the same parameters set, we can see that C' is lowered by the angular-dependence of the d-bonding. The values obtained for C_{44} are lower than the experimental data in both cases. This results for C_{44} indicate that the effect of the angular-dependence of the bonding must exists but should be more complex than I have expected.

Table 6.2 Calculated elastic constants and results of the fitting of the bulk modulus and the interatomic separations for Al_2Nd at 300K obtained by non-pairwise and pairwise potentials using a same parameters set shown in table 6.1. Presented also are the experimental data for the elastic constants [1] and the interatomic separations calculated from the experimental lattice constant data [11].

	non-pairwise	pairwise	experimental
C_{11} [GPa]	141	150	141
C_{12} [GPa]	47.2	42.6	47.0
C_{44} [GPa]	36.9	39.3	42.8
B [GPa]	78.3	78.3	78.3
C' [GPa]	46.7	53.5	47.0
$d_{\mathrm{Al-Al}}$ [a.u.]	5.3453	5.3453	5.3453
$d_{\mathrm{Al-Nd}}$ [a.u.]	6.2679	6.2679	6.2679
$d_{\mathrm{Nd-Nd}}$ [a.u.]	6.5465	6.5465	6.5466

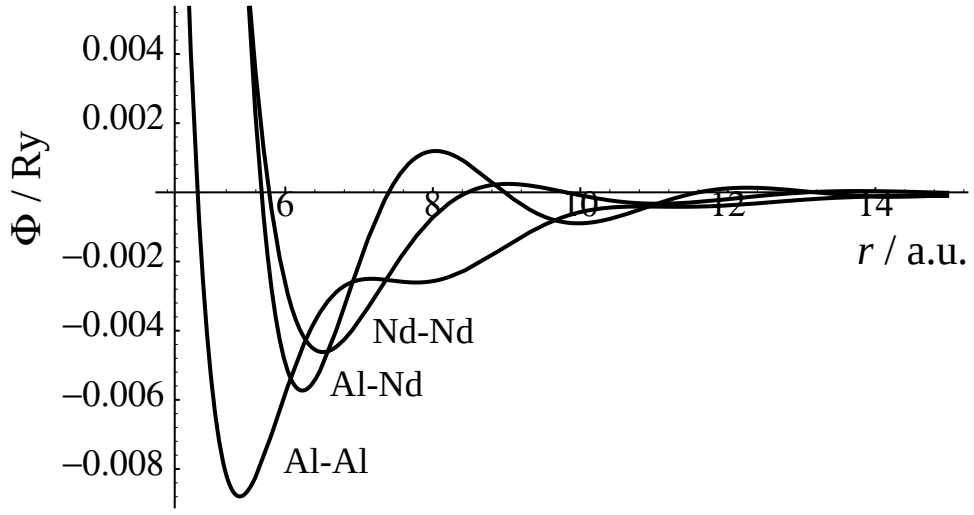

Figure 6.1 Interatomic potential for Al_2Nd calculated with the final set of parameters.

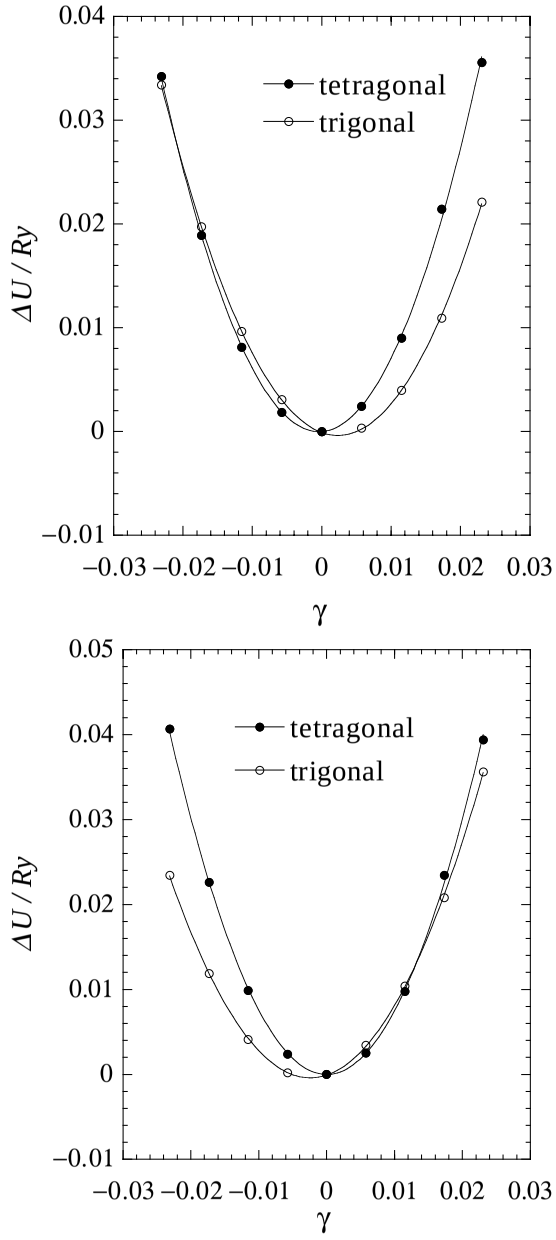

Figure 6.2 Change of the binding energy per atom as function of γ for tetragonally and trigonally deformed Al_2Nd using non-pairwise potential (upper panel) and pairwise potential (lower panel). The curves given are second-order polynomial fits.

6.3.2 Interatomic Potentials for Al_2Pr

For Al_2Pr case, the values set for the numbers of valence electrons are $N_{\mathrm{s,Al}}$ as 2.77 and derived $N_{\mathrm{d,Al}} = 0.23$, $N_{\mathrm{s,Nd}} = 1.70$ and $N_{\mathrm{d,Nd}} = 1.30$.

The adjusted parameters are compiled in table 6.3 and results of the fittings are compiled in table 6.4. The experimental data used are those at room temperature.

Table 6.3 Adjusted interatomic potential parameters for Al_2Pr phase at 300K.

	Al-Al	Al-Nd	Nd-Nd
r_{c} [Å]	0.74258	0.84392	0.91063
D	0.40489	0.08549	0.37764
r_{d} [Å]	1.19346	0.86592	0.62827

Table 6.4 Calculated elastic constants and results of the fitting of the bulk modulus and the interatomic separations for Al_2Pr at 300K obtained by non-pairwise and pairwise potentials using a same parameters set shown in table 6.3. Presented also are the experimental data for the elastic constants [1] and the interatomic separations calculated from the experimental lattice constant data [11].

	non-pairwise	pairwise	experimental
C_{11} [GPa]	136	143	138
C_{12} [GPa]	42.7	39.5	41.8
C_{44} [GPa]	34.7	36.0	45.2
B [GPa]	73.9	73.9	73.9
C' [GPa]	46.8	51.6	48.1
$d_{\mathrm{Al-Al}}$ [a.u.]	5.361	5.361	5.361
$d_{\mathrm{Al-Pr}}$ [a.u.]	6.286	6.286	6.286
$d_{\mathrm{Pr-Pr}}$ [a.u.]	6.566	6.566	6.566

The calculated elastic constants data are also compiled in table 6.4 and the changes of the binding energy curve against deformations used for the evaluations of the elastic constants are shown in figure 6.3.

The discrepancies between the calculated and the experimental C_{44} is more clearly seen compared with the Al_2Nd case as shown in table 6.4. As the experimental elastic constants data for the most of the aluminium–rare-earth cubic Laves phase intermetallic compounds highly negative Cauchy pressures are reported at

room temperature [1], the angular-dependence of the bondings in these phases must have a considerable many-atom character including Al_2Pr case.

6.4 Conclusions

Presented in this chapter is a procedure for constructing hybridized NFE-TBB potentials for binary intermetallic compounds from those for the constituent elements metals, taking Al-M (M =Nd, Pr) cubic Laves phase as an example.

The agreements of the calculated and the experimental data for the elastic constants are successfully achieved through fitting to the bulk moduli and the interatomic separations, using tight-binding parameters for the pure metals and adjusting pseudopotential parameters.

The reproducibility of the C' shows that the angular-dependent d-bond models used in the present study is physically appropriate for the bondings between aluminium atoms and rare-earth atoms in the intermetallic compounds also, and suggests at the same time that the bondings must have a considerable many-atom character.

I believe that the very simplified angular-dependent interatomic potentials model like this can be used in the intensive molecular dynamics simulations if we choose appropriate materials to study.

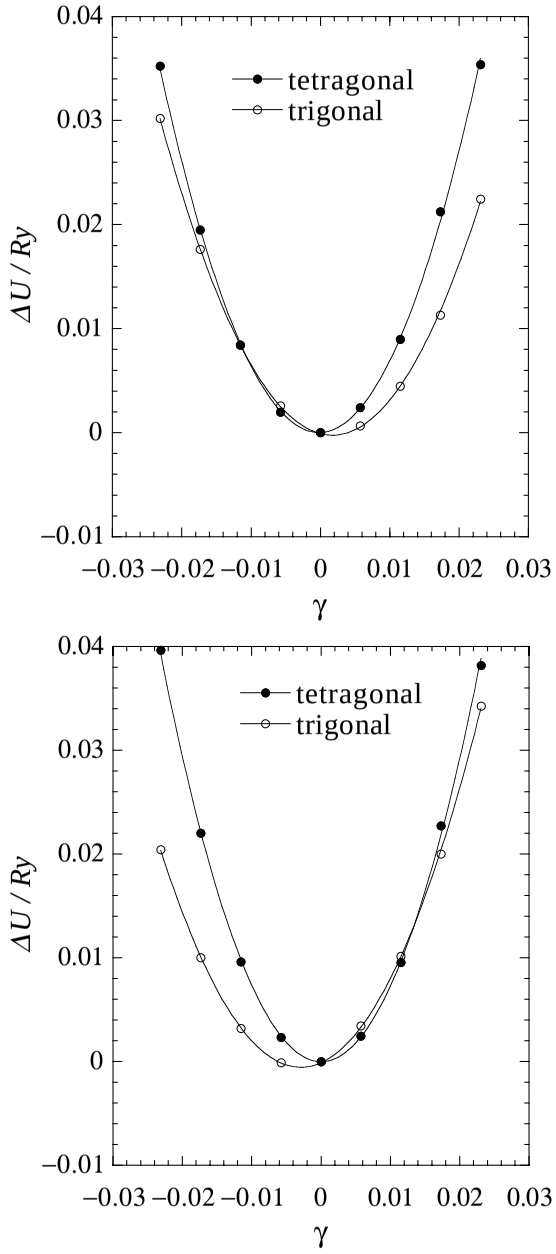

Figure 6.3 Change of the binding energy per atom as function of γ for tetragonally and trigonally deformed Al_2Pr using non-pairwise potential (upper panel) and pairwise potential (lower panel). The curves given are second-order polynomial fits.

References

[1] A. G. Every and A. H. McCurdy, *Landolt-Börnstein, New Series* Vol. III/29a, edited by O. Madelung and D. F. Nelson (Springer-Verlag, Berlin, 1992).

[2] Ch. Hausleitner and J. Hafner, *Phys. Rev.* B**45** 115 (1992).

[3] D. G. Pettifor, *Bonding and Structure of Molecules and Solids* (Oxford University Press, Oxford, 1995).

[4] S. R. Nishitani, P. Alinaghian, C. Hausleitner and D. G. Pettifor, *Phil. Mag. Lett.* **69** 177 (1994).

[5] D. G. Pettifor and M. A. Ward, *Solid State Commun.* **49** 291 (1984).

[6] N. Singh, N. S. Banger and S. P. Singh, *Phys. Rev.* B**39** 3097 (1989).

[7] J. M. Wills and W. A. Harrison, *Phys. Rev.* B**28** 4363 (1983).

[8] W. A. Harrison, *Electronic Structure and the Properties of Solids* (Freeman, San Francisco, 1980) .

[9] P. Alinaghian, S. R. Nishitani and D. G. Pettifor, *Phil. Mag.* B**69** 889 (1994).

[10] K. Hachiya and Y. Ito, *J. Alloys Compounds* **279** 171 (1998).

[11] P. Villars and L. D. Calvert, *Pearson's Handbook of Crystallographic Data for Intermetallic Phases, 2nd ed.* (ASM International, Materials Park, 1991).

Chapter 7

General conclusion

The present dissertation has accounted for the bonding and diffusional dynamics of d- and f-shell metals and their compounds through hybridized nearly-free-electron tight-binding-bond model.

Present in chapter 2 is a molecular dynamics study of the diffusion phenomena in Ni_2Y, transition-metal intermetallic phase via hybridized NFE-TBB interatomic interaction model. Interpretations of the dynamic structures from the calculations of the mean square displacements and spectral densities of velocity showed that the rapid growth of this intermetallic phase found in the experimental study is mainly due to the high-rate self-diffusion in and near the grain-boundaries and independent to the vacancy. Therefore the standard vacancy-based diffusion process is found to be not essential in this phase.

Presented in chapter 3 are first-nearest-neighbour interatomic potentials within a framework of the hybridized NFE-TBB model. Angular-dependence of the potential is included as a very simple form to account for the directional f-bonding interactions. Parameters are adjusted to reproduce the experimental interatomic separation and the bulk modulus of the fcc Th (α phase) and Pu (δ phase). Elastic constants are calculated and compared with the available experimental data. The derived potential gives a very good agreement with the experimental data for all the calculated elastic constants for fcc Th, and for the bulk modulus and the tetragonal shear modulus for fcc Pu.

Presented in chapter 4 is a procedure for deriving a simple but realistic angular-dependent hybridized NFE-TBB potential for Al. Including the properties of the d-state for the first-nearest-neighbour interactions only, very good agreements of the calculated elastic constants with the experimental data are accomplished. The reproducibility of the elastic constants has proved to depend strongly on the

angular-dependence of the d-bonding, not on the range of the interatomic interactions, while the energy difference between the different structure type depend on the range of the interactions. The NFE part of the potential, which describes the bonding properties of the sp-state and prevails over a distance, gives the correct order of the structural stability among bcc, hcp and fcc, if we take up to the fourth-nearest-neighbour interactions into account.

Presented in chapter 5 are semi-empirical interatomic potentials for the rare-earth metals (Sc, Y, La and lanthanides) and their compounds within a framework of the hybridized NFE-TBB model. Potential parameters are adjusted to reproduce the experimental data for interatomic spacings and elastic constants. The derived potentials are found to provide good agreement with the experimental data for the fcc, hcp and dhcp elemental rare-earth metals. Comparison is also made between the bond-angle dependent tight-binding d-bond model and the bond-angle independent model. The bondings in the rare-earth metals have found to do depend on the bond angles, but this is not so clearly shown as those in the transition metals.

Presented in chapter 6 is a procedure for deriving interatomic potentials for Al_2M (M =Nd, Pr) Laves phase intermetallic compounds within the framework of the hybridized NFE-TBB model. TB parameters are transferred from pure metals and pseudopotential parameters are adjusted and the total interatomic potentials with the final set of the parameters can reproduce the experimentally observed interatomic separations and bulk moduli. The three cubic elastic constants are also evaluated and compared with the experimental single-crystal data. The agreement of the calculated and the experimental data is achieved through the redistribution of the valence electrons in each atom.

As shown in these chapters, bondings in d- and f-shell metals and their compounds, described by the same or similar interatomic interaction model for the transition-metals or alloys, are largely determined by the short-range detailed structure around them, as the equilibrium interatomic separations which are determined by the first-derivative of the potential, and the elastic constants which are determined by the second-derivative of the potential, are reproduced by the short-ranged potentials. The exception for this fact is the structural energy difference, which is determined by the weak but long-ranged Friedel oscillation [1].

The short-range structure which affects the cohesive properties of these materials is not only the coordination number, but the bond-angles, as I have shown through the comparison between the angular-dependent non-pairwise potentials and the pairwise potentials depend only on the coordination numbers and the bond-angles only at the equilibrium arrangements of the nearest-neighbours.

I believe that the results and the knowledges accumulated in the present study are important for the modelling of the dynamics and the mechanical properties of the variety of materials through atomistic simulations. As the scale of the system studied through the atomistic simulations is getting larger and larger [2, 3], the importance of the semi-empirical potentials study of such large systems must become greater together with the first-principles simulations of the smaller systems.

References

[1] J. Friedel, *Phil. Mag.* **43** 153 (1952).

[2] S. J. Zhou, D. M. Beazley, P. S. Lomdahl and B. L. Holian, *Phys. Rev. Lett.* **78** 479 (1997); S. J. Zhou, D. L. Preston, P. S. Lomdahl and D. M. Beazley, *Science* **279** 1525 (1998).

[3] V. Bulatov, F. F. Abraham, L. Kubin, B. Devincre and S. Yip, *Nature* **391** 669 (1998).

List of publications

- Chapter 2
  Kan Hachiya and Yasuhiko Ito
  Molecular dynamics simulations of the self-diffusion phenomena in Ni_2Y intermetallic phase
  J. Alloys Compounds **279** 171 (1998)

- Chapter 3
  Kan Hachiya and Yasuhiko Ito
  First-nearest-neighbour interatomic potentials for light-actinide metals
  Physica B **262** 233 (1999).

- Chapter 4
  Kan Hachiya and Yasuhiko Ito
  Hybridized nearly-free-electron–tight-binding-bond interatomic potentials for aluminium
  Phil. Mag. B, submitted.

- Chapter 5
  Kan Hachiya and Yasuhiko Ito
  Interatomic potentials for rare-earth metals
  Physica B, submitted.

- Chapter 6
  Kan Hachiya and Yasuhiko Ito
  Hybridized nearly-free-electron–tight-binding-bond interatomic potentials for aluminium–rare-earth Laves phase intermetallic compounds
  Physica B, to be submitted.

Appendix A

Distribution of the valence electrons in binary transition-metal alloys

On alloying with two metal elements, the change in the electronic structure of the system takes place and this is characterized by the shift of the energy levels and the change in the band shape of each atom.

Before we start the calculation of the interatomic interactions, we must consider the redistribution of the valence electrons due to the change in the electronic structure, which is accompanied by the intra-atomic or inter-atomic electron transfer. Here, a procedure is presented for evaluating the number of the valence electrons of the constituent elements in binary A-B transition-metal alloys from those of the A and B pure metals by the set of constraints and the equation presented in the literature by Hausleitner and Hafner [1], combined with the application of the simplified approximation to the shape of the d-bands.

The rectangular band model of Friedel [2] is used for the shape of the d-bands. This is the drastic simplification of the shape of the d-bands, which assumes that the density of states are constant throughout the band width, though it is sufficient for the evaluation of the d-band occupancy (number of valence electrons in d-band) as is shown by Harrison [3]. Even with this simplified model, the trend in the variation in some properties can be explained along with the d-band occupancy, such as cohesive energy, bulk modulus, Wigner-Seitz radius, for example, especially successfully for 4d transition-metals [3].

Within this model, the change in the band shape corresponds to the change in the band width due to the change in the bondings of an atom.

The shift in the number of valence electrons $\Delta N_{l,\alpha}$ $(= N_{l,\alpha} - N^0_{l,\alpha}, \quad l = \mathrm{s}, \mathrm{d})$

is evaluated under the following constraints:

$$\Delta N_{\mathrm{s},\alpha} + \Delta N_{\mathrm{d},\alpha} = 0 \quad (\alpha = A, B), \tag{A.1}$$

$$x_A \Delta N_{\mathrm{d},A} + x_B \Delta N_{\mathrm{d},B} = 0. \tag{A.2}$$

Under these constraints, shift in the d-band energy (site-diagonal energy) $\Delta E_\alpha (= \epsilon_{\mathrm{d},\alpha} - \epsilon^0_{\mathrm{d},\alpha})$ and the difference between the A-B energy level $\Delta E (= \epsilon_{\mathrm{d},A} - \epsilon_{\mathrm{d},B})$ are given as follows:

$$\Delta E_\alpha = u_{\mathrm{dd}} \Delta N_{\mathrm{d},\alpha} + u_{\mathrm{sd}} \Delta N_{\mathrm{s},\alpha} \quad (\alpha = A, B), \tag{A.3}$$

$$\Delta E = \Delta E^0 + \Delta E_A + \Delta E_B, \tag{A.4}$$

where values for u_{dd} and u_{sd} are given in the literature [4]. Variables with a superscript, 0, are those for the pure metals elements and without a superscript are the variables for the elements in an alloy.

Schematic for the alloy d-band formation process within the rectangular d-band model is given th figure A.1. As we see from the figure, ΔE is written by the band width and the number of valence electrons as follows:

$$\begin{aligned} \Delta E &= \frac{1}{2} W_{\mathrm{d},A} - \left(\frac{1}{2} W_{\mathrm{d},B} + \frac{N_{\mathrm{d},A}}{10} W_{\mathrm{d},A} - \frac{N_{\mathrm{d},B}}{10} W_{\mathrm{d},B} \right) \\ &= \frac{1}{2} (W_{\mathrm{d},A} - W_{\mathrm{d},B}) + \frac{1}{10} \left(W_{\mathrm{d},A} N_{\mathrm{d},A} + W_{\mathrm{d},B} N_{\mathrm{d},B} \right), \end{aligned} \tag{A.5}$$

where W_{d} is the d-band width.

Band width is expressed with the d-d matrix elements and their formulation is given by Wills and Harrison [5]. The d-d matrix ddm is determined by the single parameter r_{d} and given as follows as a function of the interatomic separation.

$$ddm(r_{ij}) = \eta_{\mathrm{dd}m} \frac{\hbar^2}{m} \frac{r_{\mathrm{d}}^3}{r_{ij}^5}, \tag{A.6}$$

where $\eta_{\mathrm{dd}m} = (-45/\pi, 30/\pi, -15/2\pi)$ for $m = (0, 1, 2) = (\sigma, \pi, \delta)$. Using ddm, W_{d} is estimated as follows:

$$W_{\mathrm{d}} = \left(\frac{12}{N_{\mathrm{a}}} \right)^{1/2} \left(\sum_i \sum_{j \neq i} \frac{1}{5} \sum_m ddm^2(r_{ij}) \right)^{1/2}, \tag{A.7}$$

where N_{a} is the number of atoms. If all sites are equivalent,

$$W_{\mathrm{d}} = \left(\frac{12}{5} \right)^{1/2} \left(\sum_{j \neq i} \sum_m ddm^2(r_{ij}) \right)^{1/2}. \tag{A.8}$$

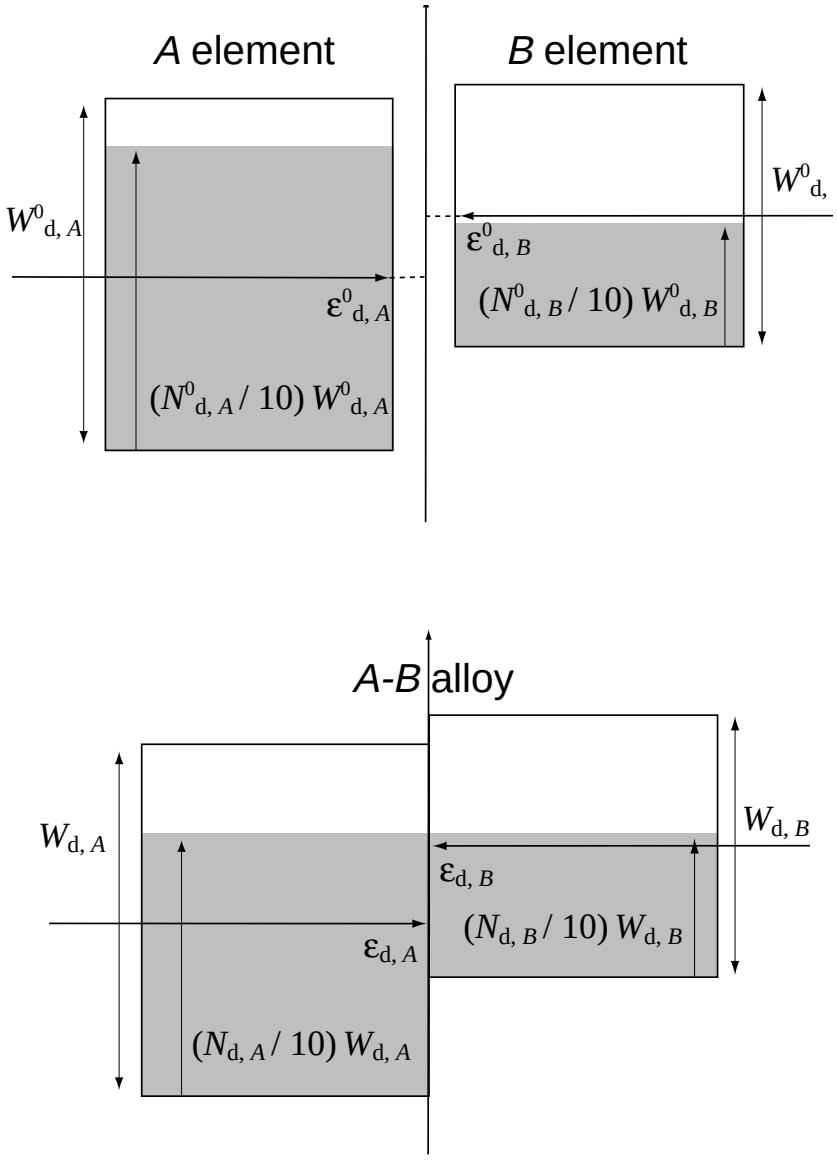

Figure A.1 Schematic of the rectangular d-band model of the binary transition-metal alloy formation.

From equations A.4 and A.5, $\Delta N_{\mathrm{d},A}$ can be derived as follows with the constraint given as equation A.2.

$$\Delta N_{\mathrm{d},A} = \frac{\frac{1}{2}(W_{\mathrm{d},A} - W_{\mathrm{d},B}) + \frac{1}{10}(W_{\mathrm{d},A}N^0_{\mathrm{d},A} + W_{\mathrm{d},B}N^0_{\mathrm{d},B}) - \Delta E^0}{\left(1 - \frac{x_A}{x_B}\right)(u_{\mathrm{dd}} - u_{\mathrm{sd}}) - \frac{1}{10}\left(W_{\mathrm{d},A} - \frac{x_A}{x_B}W_{\mathrm{d},B}\right)}. \quad \text{(A.9)}$$

This can be evaluated once we derive the d-band width. The remaining numbers of electrons, $\Delta N_{\mathrm{d},B}$, $\Delta N_{\mathrm{s},A}$ and $\Delta N_{\mathrm{s},B}$, are determined from equation A.1 and equation A.2, and the numbers of the valence electrons for the A and B elements in an A-B alloy, $N_{l,\alpha}$, are given as the sum of the pure metal numbers of the valence electrons, $N^0_{l,\alpha}$, and the shift in the numbers of valence electrons, $\Delta N_{l,\alpha}$.

References

[1] Ch. Hausleitner and J. Hafner, *Phys. Rev.* B**45** 115 (1992).

[2] J. Friedel, *The Physics of Metals*, edited by J. M. Ziman (Cambridge University Press, New York, 1969), Vol. 1, p. 340.

[3] W. A. Harrison, *Electronic Structure and the Properties of Solids* (Freeman, San Francisco, 1980).

[4] D. Nguyen-Manh, D. Mayou, A. Pasturel and F. Cyrot-Lackmann, *J. Phys.* F**15** 1911 (1985).

[5] J. M. Wills and W. A. Harrison, *Phys. Rev.* B**28** 4363 (1983).

Appendix B

Tight-binding approximations of the vacancy formation energy in binary transition-metal alloys

It is well known that the binding energy for the metallic bond system exhibits the square-root dependence on the coordination number. Vacancy formation energy, also, is affected by this fact because it is directly connected to the change in the binding energy near the vacancy and this is interpreted by a simplified semi-empirical theory [1] using such as the embedded atom potential [2]. Here, a simplified formulation for the vacancy formation energy in pure metal is extended to the alloy system straightly and demonstrate an application to the Ni_2Y intermetallic phase using hybridized nearly-free-electron–tight-binding-bond (NFE-TBB) potential.

Vacancy formation energy for binary AB compounds is estimated within nearest neighbour interaction approximation by following equation;

$$\begin{aligned} &E_{\mathrm{V,A}} = -\frac{1}{2}\left(z_{\mathrm{AA}}U_{\mathrm{AA}} + z_{\mathrm{AB}}U_{\mathrm{AB}}\right) \\ &-2\sum_{\alpha}\left[Z_{\mathrm{AA}}h_{\mathrm{AA}}\Delta\Theta^{\alpha}_{\mathrm{AA}} + Z_{\mathrm{BB}}h_{\mathrm{BB}}\Delta\Theta^{\alpha}_{\mathrm{BB}} + Z_{\mathrm{AB}}h_{\mathrm{AB}}\Delta\Theta^{\alpha}_{\mathrm{AB}}\right] \qquad \text{(B.1)} \\ &(\Delta\Theta^{\alpha}_{ij} \equiv \Theta^{\alpha,\mathrm{V}}_{ij} - \Theta^{\alpha}_{ij}, \quad i,j = \mathrm{A},\mathrm{B}) \end{aligned}$$

$E_{\mathrm{V,A}}$ is the formation energy of the A atom vacancy, h is the bond integral, Z is the coordination number, Θ^{α} is the bond order for α bond and Θ^{α} with superscript V is for the vacancy structure. Hybridized NFE-TBB interatomic potential is used for U.

In fact, the straightforward extension of the formulation for the pure metals does not give a exact estimate for the binary alloy. It is usually calculated with the chemical potentials of the species [3] to obtain vacancy concentration. The formulation presented here serves as a simple theory for the intuitive understanding of the direct connection between the vacancy formation and the bondings near the vacancy, and as a test for the convergence of the bond order.

Bond orders are calculated using the crystallographic structure of Ni_2Y (C15). The supercell for calculation contains $3 \times 3 \times 3$ unit cells and the bondings in the single unit cell at the centre of the supercell are used for the calculations. The atomic positions are fixed for all calculations and no relaxation is done. Calculated $E_{\mathrm{V,A}}$ for Ni and Y are tabulated in table B.1 up to sixth moment. Both Ni and Y vacancy have large formation energy and it is shown that more energy is needed for Y vacancy formation than for Ni vacancy formation at any approximation level.

Table B.1 Vacancy formation energy for Ni and Y in Ni_2Y phase for the M-th moment approximation.

M	2	3	4	4	6
$E_{\mathrm{V,Ni}}$	0.2302	0.1667	0.1695	0.1891	0.1376
$E_{\mathrm{V,Y}}$	0.4547	0.3117	0.1978	0.1629	0.5865

As for Ni vacancy formation energy, these values approximately corresponds to the concentrations of 10^{-15} at 773K in thermal equilibrium and therefore there are virtually very little, especially Y, vacancies.

Bond order change before and after the Ni or Y formation for the bondings near vacancies within second moment approximation is shown in figure B.1. No changes are observed for the back bondings and only bondings surrounding vacancies are strengthened.

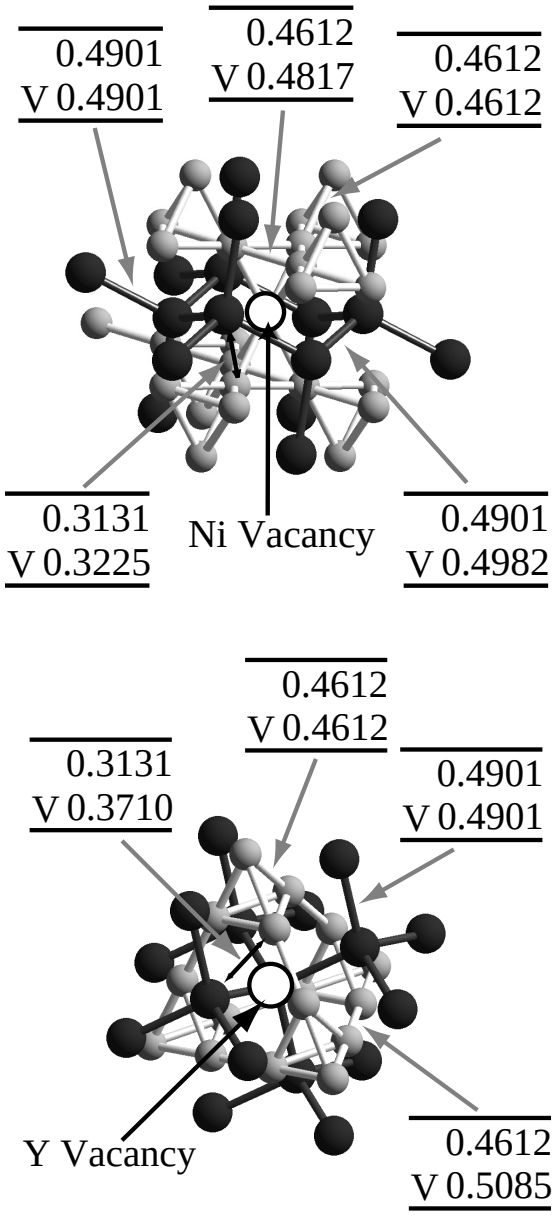

Figure B.1 Bond order change for the bondings near Ni and Y vacancy within second moment approximation. The values headed by 'V' are the bond order after vacancy formation.

References

[1] D. G. Pettifor, *Bonding and Structure of Molecules and Solids* (Oxford University Press, Oxford, 1995).

[2] M. S. Daw and M. I. Baskes, *Phys. Rev.* B**29** 1285 (1984),
M. W. Finnis and J. E. Sinclair, *Phil. Mag.* A**50** 45 (1984).

[3] C. L. Fu, Y.-Y. Ye, M. H. Ho and K. M. Ho, *Phys. Rev.* B**48** 6712 (1993).